Bifurcation map of periodic and quasi-periodic orbits around the asteroid 433 Eros using the harmonic balance method

Nicolas LECLERE, Gaëtan KERSCHEN[a]

[a]*University of Liège, Space Stuctures and Systems Laboratory (S3L), Allée de la Découverte 9, Liège, 4000, Belgium*

Abstract

This study applies the harmonic balance method (HBM) to compute and analyze periodic and quasi-periodic orbits around the asteroid 433 Eros. Traditional time-integration techniques are often computationally intensive and prone to numerical drift, particularly in the presence of instabilities or during the continuation of complex orbit families. By working directly in the frequency domain, HBM avoids these issues and offers a global, efficient framework for orbit computation. The use of the polyhedron gravity model ensures accurate modeling of Eros's irregular gravitational field, while Hill's method provides insight into the stability of periodic solutions. The study presents a dense bifurcation map highlighting over 100 bifurcations, including period-doubling and Neimark–Sacker types. A detailed spectral analysis of resonant and bifurcated orbits is conducted via normalized Fourier coefficients, offering new perspectives on orbital transitions and instabilities. The multi-harmonic extension (MHBM) is also employed to compute quasi-periodic orbits, with validation against time-domain solutions. The results demonstrate that HBM is a powerful alternative to traditional techniques, enabling accurate, efficient, and insightful analysis of complex orbital dynamics in asteroid environments.

Keywords: Asteroid, Harmonic balance method, Stability, Quasi-periodic, Periodic, Resonance

1. Introduction

Interest in small celestial bodies has grown significantly in recent years, driven by a surge of space missions focused on asteroids and comets. Notable examples include ESA's Rosetta mission, which successfully landed on comet 67P/Churyumov-Gerasimenko in 2014 [1]; NASA's Psyche mission, launched in 2023, which will be the first to orbit a metal-rich asteroid, 16 Psyche [2]; and Lucy, launched in 2021, which has already flown by two asteroids and is expected to visit nine additional Trojan asteroids near Jupiter's Lagrange points [3]. Other landmark missions include OSIRIS-REx, which collected samples from asteroid 101955 Bennu and returned them to Earth in 2023 [4]; Japan's Hayabusa2, which retrieved material from asteroid Ryugu and brought it back in 2020 [5]; and DART, the first mission aimed at testing planetary defense strategies, which successfully altered the orbit of asteroid Dimorphos in 2022 [6]. ESA's Hera mission is set to follow up on DART's impact by studying the resulting changes in 2026 [7].

Accurate mission planning around such bodies requires a solid understanding of their dynamical environments. Several techniques are available to approximate the gravitational field, including the mascon method [8], the polyhedron method [9], and a hybrid approach using tetrahedral elements [10]. The mascon method models the mass distribution as a collection of point masses, which is straightforward to apply but can lose accuracy due to gaps between the discrete elements. The tetrahedron method improves on this by dividing the volume into solid elements, reducing the impact of such voids. The polyhedron model [11; 12], used in this study, represents the body using a surface mesh under the assumption of uniform density. This approach delivers high accuracy in gravitational modeling, though the computational cost increases with mesh resolution. Nonetheless, the use of parallel computing can significantly reduce the processing time.

Identifying periodic orbits is a key part of spacecraft trajectory design. Early research by Riaguas et al. [13] showed that periodic orbits can exist around a simple linear segment. Scheeres [14] later computed several periodic orbits around asteroid 4769 Castalia by combining the Newton-Raphson method with Poincaré maps. Further studies explored periodic motion around asteroids like 216 Kleopatra and 4179 Toutatis, led by Yu [15] and Scheeres [16], respectively. Yu also introduced a hierarchical grid search technique, which was later adopted by Jiang [17] to compute near-surface periodic orbits for asteroids 216 Kleopatra and 101955 Bennu. Despite their effectiveness, these grid-based methods can be computationally intensive, especially when used with the polyhedron gravity model. To reduce this cost, Shang [18] proposed a modified approach that relies on mascon modeling along with global optimization and local refinement techniques. In 2024, Krishna [19] proposed a Legendre-Gauss collocation-based method to compute high-period orbits.

The gravitational environment near asteroids is often complex and can also support the existence of quasi-periodic orbits. Recent studies have focused on identifying these orbits, par-

ticularly around slowly rotating asteroids and small planetary moons, leading to the idea of quasi-frozen orbits [20; 21; 22]. In 2018, Baresi [23] introduced a time-domain numerical method to continue families of quasi-periodic orbits. This approach was extended in 2023 to compute two-dimensional quasi-periodic tori around planetary bodies such as Io and Phobos [24].

The search for periodic and quasi-periodic orbits often relies on time-integration methods, which tend to be computationally demanding. This work explores the use of the harmonic balance method (HBM) to identify periodic orbits around asteroid 433 Eros, by working directly in the frequency domain. By avoiding transient integration, HBM efficiently captures steady-state behavior. The method assumes that periodic solutions can be approximated by a truncated Fourier series, which is then substituted into the governing differential equations. Projecting the resulting expressions onto harmonic basis functions yields a system of nonlinear algebraic equations for the Fourier coefficients. This approach has proven particularly effective in analyzing oscillatory systems in electrical and mechanical engineering. HBM is best suited to problems where the solution remains relatively smooth, as the method becomes less efficient when strong nonlinearities introduce a wide range of harmonics—requiring more terms in the Fourier expansion to maintain accuracy. A comparative study between HBM and the collocation method on stiff systems was presented by Karkar in 2014 [25], while more recent developments and applications are reviewed by Yan [26]. Numerous examples of HBM applied to both forced and autonomous systems can be found in the literature [27; 28].

Stability analysis plays a critical role in understanding nonlinear dynamics. Hill's method offers a well-established framework for assessing the stability of linear systems with periodic coefficients. By approximating the Floquet exponents, it enables the identification of stability boundaries [29]. Bifurcation theory complements this by describing how qualitative changes in system behavior emerge as parameters vary. Bifurcations mark critical transitions where the number or nature of solutions shifts—often leading to new regimes such as periodic, quasi-periodic, or even chaotic motion. The combination of Hill's method and bifurcation analysis provides a deeper understanding of the system's behavior.

In contrast to time-marching approaches like multiple shooting or collocation, which integrate the equations of motion step by step, HBM formulates the problem entirely in the frequency domain. This avoids the accumulation of numerical errors and offers a global view of the solution from the outset. For smooth, closed orbits, accurate results can often be achieved with only a few harmonics, making HBM a valuable tool for initial analyses and continuation studies. Its ability to handle nonlinearities and assess stability without time integration is particularly advantageous in the complex environment near irregular bodies like asteroids.

This study applies the polyhedron model for gravitational modeling and introduces the HBM for the first time to study the motion of bodies around asteroids. The method is illustrated using asteroid 433 Eros, a well-characterized and irregularly shaped body. Stability is assessed using Hill's method, and quasi-periodic orbits are investigated through the multi-harmonic balance method (MHBM). The impact of harmonic content in the Fourier decomposition is compared with results from time-integration, and multiple mesh resolutions are tested to evaluate the method's adaptability across different asteroid shapes. A detailed bifurcation map of periodic orbits around 433 Eros is presented, revealing a rich structure of bifurcations and interconnected solutions. The evolution of Fourier coefficients across these families offers valuable insights into orbital dynamics. Resonant orbits are also explored, with particular attention given to transitions between directly connected resonant families. Finally, quasi-periodic orbits are computed around 433 Eros and benchmarked against time-integrated trajectories.

2. Equation of motion and polyhedron method

The polyhedron method [9] models an asteroid's gravitational field by combining geometric properties from its surface mesh. In what follows, the expressions used to compute face and edge contributions to the potential are outlined.

Each face f, of the polyhedron is associated with an outward-pointing unit normal vector $\hat{\mathbf{n}}_f$, which is essential in the computation of the matrix $\mathbf{F}_f$ where the operator $\otimes$ is the Kronecker tensor product:

$$\mathbf{F}_f = \hat{\mathbf{n}}_f \otimes \hat{\mathbf{n}}_f \tag{1}$$

Each edge e, also has an associated unit normal vector, $\hat{\mathbf{n}}_e^f$, defined with respect to a given face f. This vector points outward from the polyhedron and is perpendicular to both the normal face $\hat{\mathbf{n}}_f$ and the direction of the edge. It is used to define the contribution of the edge to the overall gravitational potential. The matrix associated with an edge defined by vertices P_1 and P_2, which lies between faces A and B, is given by

$$\mathbf{E}_{12} = \hat{\mathbf{n}}_A \otimes \hat{\mathbf{n}}_{12}^A + \hat{\mathbf{n}}_B \otimes \hat{\mathbf{n}}_{21}^B \tag{2}$$

The gravitational potential U of a polyhedron is expressed as

$$U = \frac{1}{2}G\sigma \sum_{e \in \text{edges}} \mathbf{r}_e \cdot \mathbf{E}_e \mathbf{r}_e \cdot L_e - \frac{1}{2}G\sigma \sum_{f \in \text{faces}} \mathbf{r}_f \cdot \mathbf{F}_f \mathbf{r}_f \cdot \omega_f \tag{3}$$

where G is the gravitational constant, with a value of $6.67430 \times 10^{-11} \text{m}^3 \text{kg}^{-1} \text{s}^{-2}$ and σ denotes the constant density of the polyhedron. The dimensionless scalars L_e and ω_f are associated with the geometric properties of the edges and faces, respectively.

$$L_e \equiv \int_e \frac{1}{r} \, ds = \int_{P_i}^{P_j} \frac{1}{r} \, ds = \ln \frac{r_i + r_j + e_{ij}}{r_i + r_j - e_{ij}} \tag{4}$$

$$\omega_f = \iint_{\text{face}} \frac{\Delta z}{r^3} \, dS = 2 \arctan \frac{\mathbf{r}_i \cdot (\mathbf{r}_j \times \mathbf{r}_k)}{r_i r_j r_k + r_i(\mathbf{r}_j \cdot \mathbf{r}_k) + r_j(\mathbf{r}_k \cdot \mathbf{r}_i) + r_k(\mathbf{r}_i \cdot \mathbf{r}_j)} \tag{5}$$

Considering a field point located at position O, the vector $\mathbf{r}_i$ connects O to the vertex P_i, and its magnitude is denoted r_i. The quantity e_{ij} represents the length of the edge connecting vertices P_i to P_j. The gradient of the gravitational potential is then expressed as

$$\nabla U = -G\sigma \sum_{e \in \text{edges}} \mathbf{E}_e \mathbf{r}_e \cdot L_e + G\sigma \sum_{f \in \text{faces}} \mathbf{F}_f \mathbf{r}_f \cdot \omega_f \tag{6}$$

The equations of motion governing the dynamics of a massless body in orbit around an non-accelerating and uniformly rotating asteroid are given by

$$\ddot{\mathbf{x}} + 2\omega_{\mathbf{a}} \times \dot{\mathbf{x}} + \omega_{\mathbf{a}} \times (\omega_{\mathbf{a}} \times \mathbf{x}) - \nabla U(\mathbf{x}) = 0 \tag{7}$$

where $\mathbf{x}$ denotes the position vector of the massless body, $\omega_{\mathbf{a}} = [0, 0, \omega_a]$ is the angular velocity of the asteroid about its principal axis of inertia, and $\nabla U(\mathbf{x})$ corresponds to the gravitational acceleration derived from equation (6). Time derivatives are indicated by dots.

The time invariance of equation (7) implies the existence of a conserved quantity: the Jacobi constant. In the rotating frame of the asteroid, it is expressed as

$$J = \frac{1}{2}\dot{\mathbf{x}} \cdot \dot{\mathbf{x}} - \frac{1}{2}(\omega_{\mathbf{a}} \times \mathbf{x}) \cdot (\omega_{\mathbf{a}} \times \mathbf{x}) - U(\mathbf{x}) \tag{8}$$

The Jacobi constant offers valuable insight into the structure of zero-velocity surfaces and the location of equilibrium points. These surfaces represent the boundaries beyond which a body, given its specific energy level, cannot travel, as doing so would require negative kinetic energy. In other words, all available kinetic energy would be converted into potential energy, leaving the body with zero velocity. Mathematically, this corresponds to rewriting equation (8) in terms of the modified potential V, such that

$$V = -\frac{1}{2}(\omega_{\mathbf{a}} \times \mathbf{x}) \cdot (\omega_{\mathbf{a}} \times \mathbf{x}) - U(\mathbf{x}) \tag{9}$$

An example of a surface mesh for the asteroid 433 Eros, constructed for the polyhedron method, is presented in Figure 1.

3. The harmonic balance method

An autonomous nonlinear dynamical system with n degrees of freedom (DOFs) is considered, governed by the general equations of motion

$$\mathbf{M}\ddot{\mathbf{x}} + \mathbf{C}\dot{\mathbf{x}} + \mathbf{K}\mathbf{x} = \mathbf{f}_{nl}(\mathbf{x}, \dot{\mathbf{x}}) \tag{10}$$

Here, in the particular case of the motion around an asteroid the matrices $\mathbf{M}, \mathbf{C}$ and $\mathbf{K}$ in equation (7) take the form
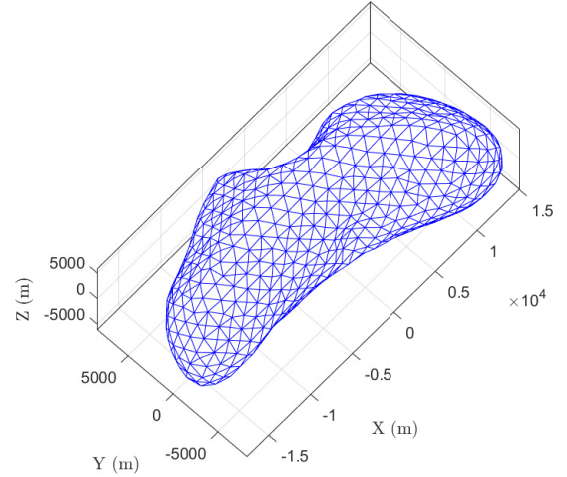

Figure 1: 3D surface mesh of asteroid 433 Eros with 856 vertices and 1708 faces.

$$\mathbf{M} = \begin{bmatrix} 1 & 0 & 0 \\ 0 & 1 & 0 \\ 0 & 0 & 1 \end{bmatrix}, \mathbf{C} = \begin{bmatrix} 0 & -2\omega_a & 0 \\ 2\omega_a & 0 & 0 \\ 0 & 0 & 0 \end{bmatrix}, \mathbf{K} = \begin{bmatrix} -\omega_a^2 & 0 & 0 \\ 0 & -\omega_a^2 & 0 \\ 0 & 0 & 0 \end{bmatrix}.$$

They are the mass, damping, and stiffness matrices, respectively. The displacement vector $\mathbf{x}$ corresponds to the 3 DOFs, and $\mathbf{f}_{nl} = \begin{bmatrix} \frac{\partial U(\mathbf{x})}{\partial x} \\ \frac{\partial U(\mathbf{x})}{\partial y} \\ \frac{\partial U(\mathbf{x})}{\partial z} \end{bmatrix}$. denotes the nonlinear force vector, computed with the polyhedron method in Eq. (6). The system is autonomous, as there is no explicit time dependence in the equations of motion. Periodic solutions are approximated using truncated Fourier series up to the N_H^{th} harmonic. Two such expansions are applied to the displacement vector $\mathbf{x}$ and the nonlinear force vector $\mathbf{f}_{nl}$ from Eq. (10):

$$\mathbf{x}(t) = \frac{\mathbf{c_0^x}}{\sqrt{2}} + \sum_{j=1}^{N_H} \left(\mathbf{s_j^x}\sin(j\omega t) + \mathbf{c_j^x}\cos(j\omega t)\right) \tag{11}$$

$$\mathbf{f}(t) = \frac{\mathbf{c_0^f}}{\sqrt{2}} + \sum_{j=1}^{N_H} \left(\mathbf{s_j^f}\sin(j\omega t) + \mathbf{c_j^f}\cos(j\omega t)\right) \tag{12}$$

Here, $\mathbf{s_j}$ and $\mathbf{c_j}$ denote the vectors of Fourier coefficients associated with the sine and cosine terms, respectively, with the superscripts $^{\mathbf{x}}$ and $^{\mathbf{f}}$ indicating displacement and force. For compact representation, these coefficients are assembled into vectors $\mathbf{z}$ and $\mathbf{b}$, respectively. The corresponding trigonometric functions—sine and cosine components across harmonics—are collected into a time-dependent vector $\mathbf{Q}(t)$.

$$\mathbf{z} = \left[\left(\mathbf{c_0^x}\right)^{\mathbf{T}}\left(\mathbf{s_1^x}\right)^{\mathbf{T}}\left(\mathbf{c_1^x}\right)^{\mathbf{T}}\ldots\left(\mathbf{s_{N_H}^x}\right)^{\mathbf{T}}\left(\mathbf{c_{N_H}^x}\right)^{\mathbf{T}}\right] \tag{13}$$

$$\mathbf{b} = \left[\left(\mathbf{c_0^f}\right)^{\mathbf{T}}\left(\mathbf{s_1^f}\right)^{\mathbf{T}}\left(\mathbf{c_1^f}\right)^{\mathbf{T}}\ldots\left(\mathbf{s_{N_H}^f}\right)^{\mathbf{T}}\left(\mathbf{c_{N_H}^f}\right)^{\mathbf{T}}\right] \tag{14}$$

$$\mathbf{Q}(t) = \begin{bmatrix} \frac{1}{\sqrt{2}} & \sin(\omega t) & \cos(\omega t) & \ldots & \sin(N_H\omega t) & \cos(N_H\omega t) \end{bmatrix} \tag{15}$$

3

By applying the Kronecker tensor product, along with the identity matrix $\mathbb{I}_3$ of dimension (3×3), Eq.(11) and Eq.(12) are written in a more compact form as Eq.(16) and (17), respectively:

$$\mathbf{x}(t) = (\mathbf{Q}(t) \otimes \mathbb{I}_3)\, \mathbf{z} \qquad (16)$$

$$\mathbf{f}(t) = (\mathbf{Q}(t) \otimes \mathbb{I}_3)\, \mathbf{b} \qquad (17)$$

This compact formulation makes it straightforward to derive expressions for velocity and acceleration directly from the vector $\mathbf{Q}(t)$:

$$\dot{\mathbf{x}}(t) = \left(\dot{\mathbf{Q}}(t) \otimes \mathbb{I}_3\right)\mathbf{z} = (\mathbf{Q}(t)\nabla \otimes \mathbb{I}_3)\,\mathbf{z} \qquad (18)$$

$$\ddot{\mathbf{x}}(t) = \left(\ddot{\mathbf{Q}}(t) \otimes \mathbb{I}_3\right)\mathbf{z} = \left(\mathbf{Q}(t)\nabla^2 \otimes \mathbb{I}_3\right)\mathbf{z} \qquad (19)$$

where ∇ is defined as the matrix

$$\nabla = \begin{bmatrix} 0 & & & & \\ & \ddots & & & \\ & & \nabla_j & & \\ & & & \ddots & \\ & & & & \nabla_{NH} \end{bmatrix}, \nabla^2 = \begin{bmatrix} 0 & & & & \\ & \ddots & & & \\ & & \nabla_j^2 & & \\ & & & \ddots & \\ & & & & \nabla_{NH}^2 \end{bmatrix} \qquad (20)$$

with

$$\nabla_j = \begin{bmatrix} 0 & -j\omega \\ j\omega & 0 \end{bmatrix}, \nabla_j^2 = \begin{bmatrix} -(j\omega)^2 & 0 \\ 0 & -(j\omega)^2 \end{bmatrix} \qquad (21)$$

Applying a Galerkin procedure to eliminate the time dependence [30] results in

$$\left(\nabla^2 \otimes \mathbf{M}\right)\mathbf{z} + (\nabla \otimes \mathbf{C})\,\mathbf{z} + (\mathbb{I}_{2N_H+1} \otimes \mathbf{K})\,\mathbf{z} = \mathbf{b} \qquad (22)$$

Finally, the system can be expressed in its most compact form within the harmonic balance framework as

$$\mathbf{h}(\mathbf{z}, \omega) = \mathbf{A}(\omega)\mathbf{z} - \mathbf{b}(\mathbf{z}) = \mathbf{0} \qquad (23)$$

Here, $\mathbf{h}(\mathbf{z}, \omega)$ denotes the residual, while the matrix $\mathbf{A}(\omega)$ encapsulates the linear dynamics of the system. Two equivalent expressions for $\mathbf{A}(\omega)$ are

$$\mathbf{A} = \nabla^2 \otimes \mathbf{M} + \nabla \otimes \mathbf{C} + \mathbb{I}_{2N_H+1} \otimes \mathbf{K} \qquad (24)$$

$$\mathbf{A} = \begin{bmatrix} \mathbf{K} & & & & & \\ & \mathbf{K} - \omega^2\mathbf{M} & -\omega\mathbf{C} & & & \\ & \omega\mathbf{C} & \mathbf{K} - \omega^2\mathbf{M} & & & \\ & & & \ddots & & \\ & & & & \mathbf{K} - (N_H\omega)^2\mathbf{M} & -N_H\omega\mathbf{C} \\ & & & & N_H\omega\mathbf{C} & \mathbf{K} - (N_H\omega)^2\mathbf{M} \end{bmatrix} \qquad (25)$$

The core idea behind Newton's method is to begin with an initial guess, $\mathbf{z}_0$, and iteratively refine it using derivative information. At each step, the next approximation $\mathbf{z}_{j+1}$ is computed using the current estimate $\mathbf{z}_j$, the residual $\mathbf{h}(\mathbf{z}_j, \omega)$, and the Jacobian with respect to $\mathbf{z}$, denoted $\mathbf{h}_\mathbf{z}(\mathbf{z}_j, \omega)$:

$$\mathbf{z}_{j+1} = \mathbf{z}_j - \mathbf{h}(\mathbf{z}_j, \omega)\mathbf{h}_\mathbf{z}^{-1}(\mathbf{z}_j, \omega) \qquad (26)$$

One of the main challenges in applying this method lies in computing the Jacobian of Eq. (23), particularly due to the nonlinear force terms. In many cases, these forces are not explicitly defined as functions of $\mathbf{z}$, which complicates the derivation. To address this, the alternative frequency–time (AFT) method can be employed to evaluate the nonlinear part of the Jacobian, specifically $\mathbf{b}(\mathbf{z})$ [31]. The AFT method leverages the discrete Fourier transform (DFT): the nonlinear forces, typically expressed in the time domain as $\mathbf{f}_{nl}(\mathbf{x}, \dot{\mathbf{x}})$, are evaluated there and then transformed back into the frequency domain to complete the computation.

$$\mathbf{z} \xrightarrow{DFT^{-1}} \mathbf{x}(t) \rightarrow \mathbf{f}_{nl}(\mathbf{x}, \dot{\mathbf{x}}) \xrightarrow{DFT} \mathbf{b}(\mathbf{z})$$

Several approaches can be used to compute the Jacobian matrix $\mathbf{h}_\mathbf{z}$. The most straightforward is the finite difference method, which is easy to implement but can be computationally expensive, especially for large systems. A more elegant and computationally efficient alternative involves interpreting the inverse Fourier transform (DFT^{-1}) as a linear operator, denoted by $\mathbf{\Gamma}(\omega)$. To reconstruct the time-domain response from its frequency-domain representation, the periodic solution (with period T) must be discretized into N time steps, with a uniform time interval $\Delta t = \frac{T}{N}$. The resulting time vector is

$$\mathbf{t} = [t_1, t_2, \ldots, t_N], \quad \text{with} \quad t_1 = 0, t_2 = \Delta t, \ldots, t_N = T - \Delta t$$

The operator $\mathbf{\Gamma}(\omega)$ then takes the form

$$\mathbf{\Gamma}(\omega) = \begin{bmatrix} \mathbb{I}_n \otimes \begin{bmatrix} 1/\sqrt{2} \\ 1/\sqrt{2} \\ \vdots \\ 1/\sqrt{2} \end{bmatrix} & \mathbb{I}_n \otimes \begin{bmatrix} \sin(\omega t_1) \\ \sin(\omega t_2) \\ \vdots \\ \sin(\omega t_N) \end{bmatrix} & \mathbb{I}_n \otimes \begin{bmatrix} \cos(\omega t_1) \\ \cos(\omega t_2) \\ \vdots \\ \cos(\omega t_N) \end{bmatrix} \cdots \\ & \mathbb{I}_n \otimes \begin{bmatrix} \sin(N_H\omega t_1) \\ \sin(N_H\omega t_2) \\ \vdots \\ \sin(N_H\omega t_N) \end{bmatrix} & \mathbb{I}_n \otimes \begin{bmatrix} \cos(N_H\omega t_1) \\ \cos(N_H\omega t_2) \\ \vdots \\ \cos(N_H\omega t_N) \end{bmatrix} \end{bmatrix} \qquad (27)$$

and links the discretized time and frequency domains

$$\tilde{\mathbf{x}} = \mathbf{\Gamma}(\omega)\mathbf{z} \qquad (28)$$

The time-domain vector $\tilde{\mathbf{x}}$, of size $3N$, is constructed by stacking the N time samples for each degree of freedom sequentially. Specifically, it is ordered as the time discretization of the first degree of freedom, followed by the second, and so on up to the 3rd, yielding

$$\tilde{\mathbf{x}} = [x_1(t_1) \ldots x_1(t_N) \ldots x_3(t_1) \ldots x_3(t_N)]$$

The inverse of Eq.(28), i.e., the direct Fourier transform, provides the relationship

4

$$\mathbf{z} = (\mathbf{\Gamma}(\omega))^+ \, \tilde{\mathbf{x}} \tag{29}$$

Here, the superscript $^+$ denotes the Moore–Penrose pseudo-inverse, given by $\mathbf{\Gamma}^+ = \mathbf{\Gamma}^\top \left(\mathbf{\Gamma} \mathbf{\Gamma}^\top \right)^{-1}$. This operator is also used to transform the nonlinear force vector, evaluated in the time domain, back into the frequency domain to compute

$$\mathbf{b}(\mathbf{z}) = (\mathbf{\Gamma}(\omega))^+ \, \tilde{\mathbf{f}} \tag{30}$$

Using Eqs. (29) and (30), the Jacobian $\mathbf{h_z}(\mathbf{z}_j, \omega)$ is conveniently expressed as

$$\mathbf{h_z} = \frac{\partial \mathbf{h}}{\partial \mathbf{z}} = \mathbf{A} - \frac{\partial \mathbf{b}}{\partial \mathbf{z}} = \mathbf{A} - \frac{\partial \mathbf{b}}{\partial \tilde{\mathbf{f}}} \frac{\partial \tilde{\mathbf{f}}}{\partial \tilde{\mathbf{x}}} \frac{\partial \tilde{\mathbf{x}}}{\partial \mathbf{z}} = \mathbf{A} - \mathbf{\Gamma}^+ \frac{\partial \tilde{\mathbf{f}}}{\partial \tilde{\mathbf{x}}} \mathbf{\Gamma} \tag{31}$$

The term $\frac{\partial \tilde{\mathbf{f}}}{\partial \tilde{\mathbf{x}}}$—the Jacobian of the nonlinear forces with respect to the state in the time domain—is easily derived from Eq. (6) [9].

3.1. Phase condition

Solutions of autonomous nonlinear systems exhibit time-translation invariance. That is, if $\phi(t)$ is a solution to an autonomous system with an initial condition $x(\Delta t) = x_0$, then the time-shifted function $\phi(t + \Delta t)$ is also a valid solution with initial condition $x(0) = x_0$. However, since the HBM operates in the frequency domain, this invariance must be expressed in terms of Fourier coefficients. To restore uniqueness, a phase condition—denoted $g(\mathbf{z})$—must be imposed. The most basic approach is to fix one of the Fourier coefficients, typically by setting a component of $\mathbf{z}$ to zero (e.g., $\mathbf{z}_i = 0$), which corresponds to constraining the initial displacement or velocity. However, this strategy can result in a phase drift during continuation, which may introduce numerical inaccuracies and slow down the computation.

A more robust and general phase condition, which does not depend on the specific type of nonlinearity, is used in continuation software like AUTO [32; 33].

$$g(\mathbf{z}) = \mathbf{z}_{j-1}^T \left(\nabla \otimes \mathbf{I}_n \right) \mathbf{z} = 0 \tag{32}$$

This condition ensures smooth progression between continuation steps by limiting abrupt changes, thus helping prevent numerical errors. Additionally, its derivative with respect to $\mathbf{z}$ aligns with the singular eigenvector φ. In other words, this phase condition effectively cancels the evolution of $\mathbf{z}$ along the null direction of the Jacobian, thereby enforcing the uniqueness of the periodic solution.

3.2. Injection of fictitious energy

Adding a phase condition to the system introduces an extra constraint, which results in an overdetermined problem and a non-square Jacobian matrix. A common workaround is to use the Moore–Penrose pseudoinverse [34]. However, a more elegant and efficient strategy is to inject a fictitious, non-conservative energy term $\mathbf{E}_{\text{fic}}$, scaled by a damping parameter μ, into the equations of motion

$$\mathbf{M}\ddot{\mathbf{x}} + \mathbf{C}\dot{\mathbf{x}} + \mu \mathbf{E}_{fic}(\dot{x}) + \mathbf{K}\mathbf{x} - \mathbf{f}_{nl}(\mathbf{x}, \dot{\mathbf{x}}) = \mathbf{0} \tag{33}$$

In order for the system to admit periodic solutions, it must be conservative when there is no external forcing. This means that the damping coefficient μ should remain zero as the continuation progresses [35]. Accordingly, the HBM formulation (Eq. (23)) becomes

$$\mathbf{h}(\mathbf{z}, \omega, \mu) = \mathbf{A}(\omega)\mathbf{z} + \mu \mathbf{P}(\mathbf{z}) - \mathbf{b}(\mathbf{z}) = \mathbf{0} \tag{34}$$

with $\mathbf{P}(\mathbf{z})$ the fictitious energy $\mathbf{E}_{fic}(\dot{x})$ expressed in the frequency domain. Since μ goes to zero during the continuation, the specific shape of $\mathbf{P}(\mathbf{z})$ is not critical—as long as it is non-conservative. That said, the choice does affect the structure of the Jacobian. Ideally, $\mathbf{P}(\mathbf{z})$ should be set equal to the phase condition vector, i.e., $\mathbf{P}(\mathbf{z}) = (\nabla \otimes \mathbf{I}_n) \mathbf{z}$. With this choice, the derivative of $\mathbf{h}$ with respect to μ denoted $\mathbf{h}_\mu$ becomes identical to $\mathbf{g_z}$, and the singularity in the Jacobian of the augmented system is naturally resolved.

3.3. Initialization and continuation

The computation of a single periodic solution for a conservative autonomous system has been detailed in the previous sections. However, in practice, it is often more insightful to compute entire branches of solutions over a range of frequencies. To achieve this, various continuation techniques are available. The MANLAB package, for instance, uses the asymptotic numerical method (ANM), while arc-length continuation is another well-established approach [36]. In this work, the chosen method follows the continuation scheme implemented in the MATCONT toolbox, which relies on a Moore–Penrose-based formulation [37].

The augmented system used for continuation couples the HBM equation (Eq. (34)) with the phase condition (Eq. (32))

$$\begin{bmatrix} \mathbf{h}(\mathbf{z}, \omega, \mu) \\ g(\mathbf{z}) \end{bmatrix} = \begin{bmatrix} \mathbf{A}(\omega)\mathbf{z} + \mu \mathbf{P}(\mathbf{z}) - \mathbf{b}(\mathbf{z}) \\ \mathbf{z}_{j-1}^T (\nabla \otimes \mathbf{I}_n) \mathbf{z} \end{bmatrix} = \begin{bmatrix} \mathbf{0} \\ 0 \end{bmatrix} \tag{35}$$

The continuation is carried out alongside a prediction step. The method adopted here is tangent prediction, where the next point on the solution branch is estimated using the tangent vector at the previous point. Let $\mathbf{t}_i$ denote the tangent vector associated with the current solution $\mathbf{y}_i = \begin{bmatrix} \mathbf{z}_i^T & \omega_i & \mu_i \end{bmatrix}^T$. This vector is obtained by solving the linear system

$$\begin{bmatrix} \mathbf{J}(\mathbf{y}_i) \\ \mathbf{G_y} \\ \mathbf{t}_{i-1}^T \end{bmatrix} \mathbf{t}_i = \begin{bmatrix} \mathbf{0} \\ 0 \\ 1 \end{bmatrix} \tag{36}$$

Here, $\mathbf{J}(\mathbf{y}_i) = \begin{bmatrix} \mathbf{h_z} & \mathbf{h}_\omega & \mathbf{h}_\mu \end{bmatrix}$ is the Jacobian of the HBM system, and $\mathbf{G_y} = \begin{bmatrix} \mathbf{g_z} & 0 & 0 \end{bmatrix}$ is the Jacobian of the phase condition. The last row in Eq. (36), $\mathbf{t}_{i-1}^T \mathbf{t}_i = 1$, enforces a unit projection onto the previous tangent, preventing the predictor

from reversing direction along the branch.

All the components of the Jacobian system have been defined in earlier sections, except for $\mathbf{h}_\omega$, which is the derivative of Eq. (34) with respect to the frequency ω, and can be obtained straightforward as

$$\mathbf{h}_\omega = \frac{\partial \mathbf{A}(\omega)}{\partial \omega} \mathbf{z} \tag{37}$$

The tangent vector is scaled by a step size s_i and added to the current solution to obtain the prediction for the next continuation point:

$$\mathbf{y}_{i+1} = \mathbf{y}_i + s_i \mathbf{t}_i \tag{38}$$

Once the prediction $\mathbf{y}_{i+1}$ is constructed, it must be corrected to satisfy the system of equations (Eq. (34)). The correction is performed using a Moore–Penrose-based method with an auxiliary optimization variable $\mathbf{v}_i$, initialized as the tangent vector $\mathbf{t}_i$. The correction update rules are

$$\mathbf{y}_{i+1}^{j+1} = \mathbf{y}_{i+1}^{j} + \Delta \mathbf{y}_{i+1}^{j} = \mathbf{y}_{i+1}^{j} - \mathbf{G_y}^{-1}(\mathbf{y}_{i+1}^{j}, \mathbf{v}_{i+1}^{j})\mathbf{G}(\mathbf{y}_{i+1}^{j}, \mathbf{v}_{i+1}^{j}) \tag{39}$$

$$\mathbf{v}_{i+1}^{j+1} = \mathbf{v}_{i+1}^{j} + \Delta \mathbf{v}_{i+1}^{j} = \mathbf{v}_{i+1}^{j} - \mathbf{G_y}^{-1}(\mathbf{y}_{i+1}^{j}, \mathbf{v}_{i+1}^{j})\mathbf{R}(\mathbf{y}_{i+1}^{j}, \mathbf{v}_{i+1}^{j}) \tag{40}$$

where the residuals and Jacobians are defined as

$$\mathbf{G}(\mathbf{y}, \mathbf{v}) = \begin{bmatrix} \mathbf{h}(\mathbf{y}) \\ g(\mathbf{y}) \\ \mathbf{0} \end{bmatrix} \tag{41}$$

$$\mathbf{G_y}(\mathbf{y}, \mathbf{v}) = \begin{bmatrix} \mathbf{J}(\mathbf{y}) \\ \mathbf{g_y}(\mathbf{y}) \\ \mathbf{v}^T \end{bmatrix} \tag{42}$$

$$\mathbf{R}(\mathbf{y}, \mathbf{v}) = \begin{bmatrix} \mathbf{J}(\mathbf{y})\mathbf{v} \\ \mathbf{g_y}(\mathbf{y})\mathbf{v} \\ \mathbf{0} \end{bmatrix} \tag{43}$$

With this prediction–correction scheme, one can trace out the evolution of the families of orbits with respect to their frequency.

3.4. Multi-harmonic balance method

A quasi-periodic orbit is characterized by the interaction of multiple frequencies, which requires adapting the classical harmonic balance method (HBM) to account for this complexity. The first adaptation of the HBM for multi-frequency systems was developed in 1981 for electrical circuits by Chua and colleagues [38]. Several years later, the method was improved through coupling with the alternative frequency–time domain method (AFT) [39]. Guillot extended the approach further by enabling the continuation of quasi-periodic solutions involving two frequencies using the asymptotic numerical method (ANM) [40]. More recently, Wang proposed an efficient adaptation of the reconstruction-based HBM for handling

multiple frequencies [41]. A detailed analysis of the quasi-periodic responses of a single degree-of-freedom harmonically forced Duffing oscillator, as well as a two-degree-of-freedom system using the MHBM—along with their respective stability properties—was provided by Liao [42].

To account for quasi-periodic solutions involving multiple incommensurate frequencies, the trajectory $\mathbf{x}(t)$ is expressed as a multi-harmonic Fourier series involving N_ω such frequencies ω_i:

$$\mathbf{x}(t) = \prod_{i=1}^{N_\omega} \left(\mathbf{Q}_i(\omega_i t) \otimes \mathbf{I}_{n_i} \right) \mathbf{z} \tag{44}$$

Here, $\mathbf{Q}_i(\omega_i t)$ denotes the Fourier basis matrix associated with the ith frequency component, constructed as

$$\mathbf{Q}_i(\omega_i t) = \left[\tfrac{1}{\sqrt{2}}, \quad \sin(\omega_i t), \quad \cos(\omega_i t), \quad \cdots, \quad \sin(N_{H_i}\omega_i t), \quad \cos(N_{H_i}\omega_i t) \right] \tag{45}$$

The dimension n_i accounts for the nested structure of the multi-frequency expansion and is defined recursively as

$$n_i = n \prod_{k=1}^{i-1} (2N_{H_k} + 1) \tag{46}$$

where n is the number of degrees of freedom of the system and N_{H_k} is the number of harmonics considered for the kth frequency.

Time derivatives of $\mathbf{x}(t)$, the velocity $\dot{\mathbf{x}}(t)$ and the acceleration $\ddot{\mathbf{x}}(t)$, are easily expressed with the Fourier series as

$$\dot{\mathbf{x}}(t) = \sum_{i=1}^{N_\omega} \left(\prod_{j=1}^{N_\omega} \left(\mathbf{Q}_j(\omega_j t)\kappa_{ji} \right) \otimes \mathbf{I}_{n_j} \right) \mathbf{z} \tag{47}$$

$$\ddot{\mathbf{x}}(t) = \sum_{i=1}^{N_\omega} \sum_{j=1}^{N_\omega} \left(\prod_{k=1}^{N_\omega} \left(\mathbf{Q}_k(\omega_k t)\kappa_{kj}\kappa_{ki} \right) \otimes \mathbf{I}_{n_k} \right) \mathbf{z} \tag{48}$$

where the derivation operator κ_{ji} is

$$\kappa_{ji} = \begin{cases} \kappa_j & \text{if } i = j \\ \mathbb{I}_{2N_{H_j}+1} & \text{if } i \neq j \end{cases}, \quad \kappa_j = \begin{bmatrix} 0 & & \mathbf{0} \\ & \begin{bmatrix} 1 & & \\ & \ddots & \\ & & N_{H_j} \end{bmatrix} & \\ \mathbf{0} & & \end{bmatrix} \otimes \kappa \quad \kappa = \begin{bmatrix} 0 & -\omega \\ \omega & 0 \end{bmatrix} \tag{49}$$

The quasi-periodic motion can be expressed by N_ω independent torus variables, $\theta_i = \omega_i t$ that allow to easily perform the Galerkin procedure in the orthogonal trigonometric basis $\mathbf{Q}_i$ where

$$\frac{1}{\pi} \int_0^{2\pi} \mathbf{Q}_i^T(\theta_i)\mathbf{Q}_i(\theta_i) \, d\theta_i = \mathbf{I}_{2N_{H_i}+1} \tag{50}$$

Eq.(10) are thus recast in the frequency domain as

$$\left[\sum_{k=1}^{N_x} \sum_{j=1}^{N_y} \left(\bigotimes_{i=N_\omega}^{1} \kappa_{ij}\kappa_{ik} \right) \otimes \mathbf{M} + \sum_{j=1}^{N_x} \left(\bigotimes_{i=N_\omega}^{1} \kappa_{ij} \right) \otimes \mathbf{C} + \left(\bigotimes_{i=N_\omega}^{1} \mathbf{I}_{2N_{H_i}+1} \right) \otimes \mathbf{K} \right] \mathbf{z} - \mathbf{b}(\mathbf{z}) = 0 \tag{51}$$

6

or in the compact form,

$$\mathbf{A}(\omega_1, \dots, \omega_{N_\omega})\mathbf{z} - \mathbf{b}(\mathbf{z}) = \mathbf{h}(\mathbf{z}) = 0 \qquad (52)$$

The matrix of the linear dynamics for two frequencies $\mathbf{A}$ is a $n(2N_{H_1}+1)(2N_{H_2}+1) \times n(2N_{H_1}+1)(2N_{H_2}+1)$. As the number of incommensurate frequencies increases, the complexity of the multi-harmonic balance method grows rapidly. Specifically, the size of matrix $\mathbf{A}$ scales with the product of the harmonic orders, resulting in a steep rise in both computational cost and memory usage. To manage this, the present study focuses on responses involving two frequencies, using 20 harmonics for the first and 10 for the second. This choice strikes a balance between computational feasibility and the ability to capture detailed and meaningful dynamical behavior near asteroid 433 Eros.

The same continuation procedure as outlined on the classical harmonic balance method is applied to solve Eq. (52). The core steps—projection, nonlinear evaluation using AFT, and continuation using pseudo arch-length remain unchanged. However, the presence of multiple incommensurate frequencies introduces additional considerations. The main difference lies in the need to account for more than one frequency in the formulation. While the primary frequency is treated as a continuation parameter, the secondary frequency must also be carefully controlled. To ensure the uniqueness of the solution and avoid redundancy due to time-shifting invariance, an additional phase condition is imposed on the secondary frequency. This phase condition effectively fixes one degree of freedom in the multi-dimensional torus of quasi-periodic motion, ensuring a well-posed system for continuation. Following the approach proposed by Schilder [43] the phase condition selected minimizes the L2 norm of the difference between the current solution and that of the previous iteration, denoted by $\mathbf{z}_{j-1}$. After the Galerkin procedure the phase condition takes the form:

$$p_i(\mathbf{z}) = \frac{1}{\omega_i} \mathbf{z}_{j-1}^T \left[\left(\bigotimes_{j=N_\omega}^{1} \kappa_{ji}^T \right) \otimes \mathbf{I}_n \right] \mathbf{z} = \mathbf{z}_{j-1}^T \hat{\mathbf{P}}_i \mathbf{z} = 0 \qquad (53)$$

A flowchart summarizing the HBM algorithm, including all previously detailed steps, is presented in Figure 2.

3.5. Stability

Nonlinear systems are subject to complex dynamical behaviors, including unstable solutions and bifurcation phenomena. In the time domain, Floquet theory provides insight into the stability of periodic solutions by analyzing the eigenvalues of the monodromy matrix. In the frequency domain, an alternative approach—Hill's method—relies on the Floquet exponent, λ, to evaluate the stability of solutions. The Floquet multipliers, σ, are related to the exponents through the relation:

$$\sigma_i = e^{\lambda_i T} \qquad (54)$$

A periodic solution is unstable if at least one Floquet multiplier satisfies $|\sigma_i| > 1$; otherwise, the solution is considered
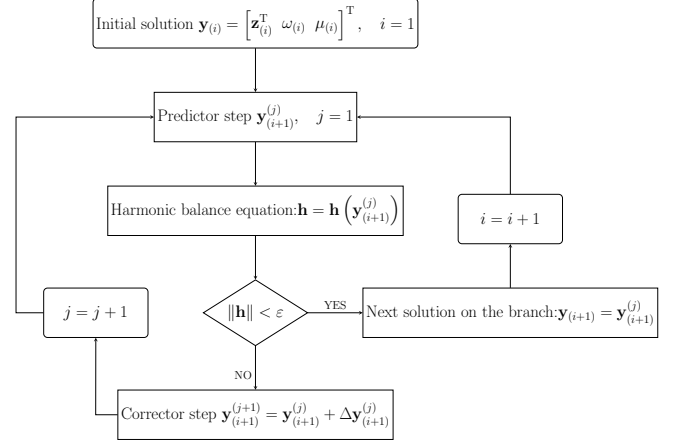

Figure 2: Algorithm flowchart of HBM.

stable. In terms of the Floquet exponents, instability occurs if the real part of any exponent satisfies $\text{Re}(\lambda_i) > 0$.

Hill's method introduces a periodic perturbation, $\mathbf{s}(t)$, modulated by an exponential term, to an existing periodic solution $\mathbf{x}^*(t)$:

$$\mathbf{p}(t) = \mathbf{x}^*(t) + e^{\lambda T}\mathbf{s}(t) \qquad (55)$$

This perturbed solution is then substituted into the equations of motion, Eq. (10), to assess the evolution and stability of the response.

$$\mathbf{M}\ddot{\mathbf{x}}^* + \mathbf{C}\dot{\mathbf{x}}^* + \mathbf{K}\mathbf{x}^* + \left(\lambda^2\mathbf{Ms} + \lambda\left(2\mathbf{M}\dot{\mathbf{s}} + \mathbf{Cs}\right) + \mathbf{M}\ddot{\mathbf{s}} + \mathbf{C}\dot{\mathbf{s}} + \mathbf{Ks}\right)e^{\lambda T} = \mathbf{f}(\mathbf{p}, \dot{\mathbf{p}}, \omega) \qquad (56)$$

Using a Fourier decomposition truncated to the Nth order for the periodic solution $\mathbf{x}(t)$ and its perturbation $\mathbf{s}(t)$, the corresponding vectors of Fourier coefficients are denoted $\mathbf{z}$ and $\mathbf{u}$, respectively. Applying the Galerkin procedure to the perturbed equations yields

$$\mathbf{Az}^* + \left(\lambda^2\Delta_2 + \lambda\Delta_1 + \mathbf{A}\right)e^{\lambda T}\mathbf{u} = \mathbf{b}\left(\mathbf{z}^* + e^{\lambda T}\mathbf{u}\right) \qquad (57)$$

where the operators Δ_1 and Δ_2 are defined as

$$\Delta_1 = \nabla \otimes 2\mathbf{M} + \mathbb{I}_{2N_H+1} \otimes \mathbf{C} \qquad (58)$$

$$\Delta_2 = \mathbb{I}_{2N_H+1} \otimes \mathbf{M} \qquad (59)$$

To simplify Eq. (57), a Taylor series expansion of the right-hand side is performed:

$$\mathbf{b}\left(\mathbf{z}^* + e^{\lambda T}\mathbf{u}\right) = \mathbf{b}(\mathbf{z}^*) + \frac{\partial \mathbf{b}}{\partial \mathbf{z}}\left(e^{\lambda T}\mathbf{u}\right) \qquad (60)$$

This makes the residual $\mathbf{Az}^* - \mathbf{b}(\mathbf{z}^*)$ appear, which vanishes by construction of the harmonic balance equation, Eq.(23). Substituting this expression and introducing the Jacobian matrix $\mathbf{h}_z$, defined in Eq.(31), leads to the following quadratic eigenvalue problem:

7

$$\left(\mathbf{\Delta_2}\lambda^2 + \mathbf{\Delta_1}\lambda + \mathbf{h_z}\right)e^{\lambda t}\mathbf{u} = \mathbf{0} \qquad (61)$$

Since the exponential term is non-zero, it can be omitted, resulting in

$$\left(\mathbf{\Delta_2}\lambda^2 + \mathbf{\Delta_1}\lambda + \mathbf{h_z}\right)\mathbf{u} = \mathbf{0} \qquad (62)$$

This quadratic eigenvalue problem can be reformulated as a linear eigenvalue problem by increasing its dimension, typically by a factor of two [30]. Among all computed eigenvalues λ, only $2n$ are meaningful as they approximate the true Floquet exponents of the periodic solution $\mathbf{x}^*$ [44]. Since the system presented in this work is Hamiltonian, the Floquet exponents appear as n reciprocal pairs. According to [45], the relevant exponents are those with the smallest imaginary parts in modulus, while the others are discarded due to their lack of physical significance.

It is worth noting that the accuracy of the computed Floquet exponents improves with the number of harmonics used in the Fourier decomposition. However, for autonomous systems, the Jacobian $\mathbf{h}_z$ is always singular due to time-translation invariance, resulting in two zero eigenvalues. These may affect the numerical conditioning of the stability analysis. Common remedies include shifting the null eigenvalues to a small negative value (e.g., -1), as suggested in [46], or simply discarding them, since they do not interfere with the detection of bifurcations.

During the continuation process, the evolution of the Floquet multipliers along the unit circle can reveal the presence of specific points known as bifurcations. Bifurcations are often associated with changes in the stability of the system; however, a stability change is not a necessary condition for a bifurcation to occur.

In the context of this work, three particular types of bifurcations are considered, namely singular points, period doubling and Neimark Sacker bifurcations. A more comprehensive treatment of bifurcation theory can be found in Kuznetsov [47]. The characteristic behavior of the Floquet exponents and multipliers for these three bifurcation types is illustrated in Figure 3.

3.6. Singular points

Singular points occur when the real part of a Floquet exponent changes sign while its imaginary part is zero. This is equivalent to a pair of Floquet multipliers entering or leaving the unit circle through the point $(1, 0)$. At such points, the Jacobian matrix $\mathbf{h_z}$ (Eq. (31)) becomes singular. Among these singular points, two types of bifurcations can arise: fold bifurcations and branch points (BP). They can be distinguished using $\mathbf{h}_\omega$ (Eq. (37)):

- Fold bifurcations satisfy $\mathbf{h}_\omega{}^T\mathbf{u} \neq 0$.

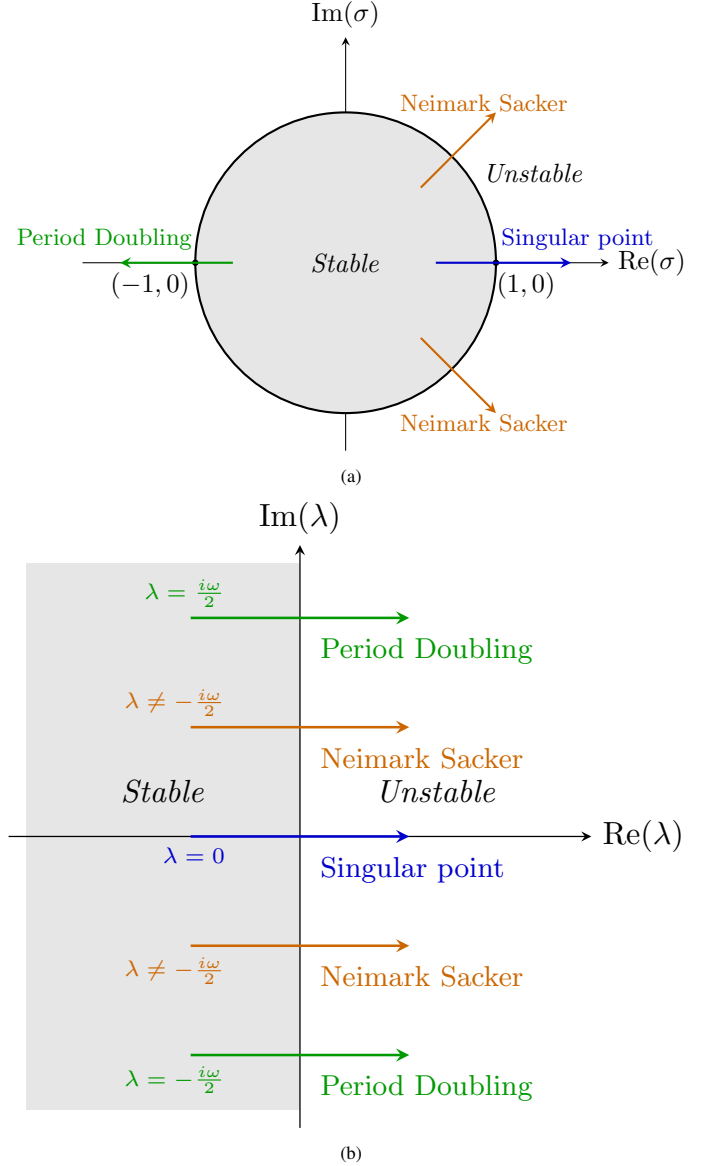- Branch points satisfy $\mathbf{h}_\omega{}^T\mathbf{u} = 0$.

Figure 3: Bifurcations with respect to the Floquet multipliers (a) and Floquet exponents (b).

Fold bifurcation : Also known as limit points or saddle nodes, folds do not give rise to new branches of solutions. They are characterized by a reversal in the direction of the continuation parameter ω, typically showing an increase followed by a decrease (or vice versa). Since folds do not introduce new solution paths, their detection is not addressed in this work.

Branch point : Before a branch point the system follows a single solution branch. After the bifurcation, multiple branches emerge. This bifurcation is often accompanied by a change in stability between the primary branch and the new one(s).

- If two branches meet and exchange stability, the phenomenon is referred to as a transcritical bifurcation.

- If a new branch emerges from the main one—either stable or unstable—along with a stability change in the main

branch, the bifurcation is termed a pitchfork bifurcation.

The singularity of $\mathbf{h_z}$ at these points can be leveraged to detect folds and branch points. In both cases, the determinant of $\mathbf{h_z}$ vanishes. To distinguish between them, the rank deficiency of the Jacobian system in Eq. (36) is exploited, as proposed in [48]. The test function used for branch point detection is

$$\varphi_i = \det \begin{pmatrix} \mathbf{h_z} & \mathbf{h}_\omega & \mathbf{h}_\mu \\ \mathbf{g_z} & 0 & 0 \\ & \mathbf{t_{i-1}^T} & \end{pmatrix} \quad (63)$$

A branch point bifurcation is identified when this test function changes sign between two consecutive continuation steps, i.e, $\varphi_i \cdot \varphi_{i+1} < 0$.

3.7. Period Doubling

Period doubling bifurcations (PD) occur when a pair of Floquet multipliers exits or enters the unit circle through the point $(-1, 0)$ on the real axis. In terms of Floquet exponents, this corresponds to a pair of complex conjugate exponents crossing the imaginary axis at $\lambda = \pm \frac{i\omega}{2}$. At the bifurcation point, a new branch of periodic solutions emerges, with the new solutions having a period twice that of the original branch.

Several test functions are available for detecting PD bifurcations; two such methods are detailed in [49]. The first method involves substituting $\lambda = \frac{i\omega}{2}$ into Eq. (62) and decomposing the associated eigenvector into its real and imaginary parts as $\mathbf{u} = \mathbf{u_R} + i\mathbf{u_I}$, yielding

$$\begin{bmatrix} \mathbf{h_z} - \left(\frac{\omega}{2}\right)^2 \mathbf{\Delta_2} & \frac{\omega}{2}\mathbf{\Delta_1} \\ -\frac{\omega}{2}\mathbf{\Delta_1} & \mathbf{h_z} - \left(\frac{\omega}{2}\right)^2 \mathbf{\Delta_2} \end{bmatrix} \begin{pmatrix} \mathbf{u_R} \\ \mathbf{u_I} \end{pmatrix} = \mathbf{B} \begin{pmatrix} \mathbf{u_R} \\ \mathbf{u_I} \end{pmatrix} = \begin{pmatrix} \mathbf{0} \\ \mathbf{0} \end{pmatrix} \quad (64)$$

The matrix on the left-hand side of this equation, denoted as $\mathbf{B}$, becomes singular at the PD bifurcation. A simple detection method relies on monitoring the sign variation of the derivative of the determinant of $\mathbf{B}$ during the continuation. Using a finite difference approximation for the derivative, the associated test function is defined as

$$\varphi_i = \det(\mathbf{B}_i) - \det(\mathbf{B}_{i-1}) \quad (65)$$

The presence of a bifurcation is indicated when the test function changes sign between two consecutive steps, i.e., when $\varphi_i \cdot \varphi_{i+1} < 0$. Alternative approaches are presented in [49]. However, these methods can occasionally yield false positives in the context of autonomous systems. Therefore, it is recommended to combine them with direct monitoring of the Floquet multipliers or exponents during the continuation to enhance robustness.

A third method, also discussed in [49], involves modifying the frequency basis by explicitly incorporating subharmonics into the Fourier decomposition. In this case, the vector $\mathbf{Q}(t)$ (as defined in Eq. (15)) is extended as

$$\mathbf{Q}_{PD}(t) = \left[\frac{1}{\sqrt{2}}, \sin\left(\frac{\omega}{2}t\right), \cos\left(\frac{\omega}{2}t\right), \sin(\omega t), \cos(\omega t), \dots \right.$$

$$\left. \sin(N_H \omega t), \cos(N_H \omega t), \sin\left(\frac{(2N_H + 1)\omega}{2}t\right), \cos\left(\frac{(2N_H + 1)\omega}{2}t\right) \right] \quad (66)$$

This modification changes the nature of the emerging branch from a PD bifurcation. The period no longer doubles; instead, in the new frequency basis, the PD bifurcation manifests as a branch point bifurcation [47]. Consequently, the established detection framework for branch points can be applied to reliably identify PD bifurcations. The downside of this approach is that the minimal period is extended from T to $2T$, and the number of unknowns in the system is effectively doubled.

3.8. Neimark Sacker

Neimark–Sacker (NS) bifurcations, also known as secondary Hopf bifurcations, occur when a pair of complex conjugate Floquet multipliers exit the unit circle. In terms of Floquet exponents, this corresponds to crossing the imaginary axis at values different from $\pm \frac{i\omega}{2}$. NS bifurcations give rise to a new branch of solutions characterized by quasiperiodic oscillations, defined by a combination of the fundamental frequency ω and at least one secondary frequency ω_2, such that the ratio $\frac{\omega}{\omega_2}$ is irrational. The resulting quasiperiodic branches require the application of the MHBM. There is no explicit test function for the detection of NS bifurcations in autonomous systems. However, in the scope of this work, all observed NS bifurcations are accompanied by a change in stability. Therefore, the presence of an NS bifurcation is inferred from a stability change where $\text{Im}(\lambda) \neq 0$, confirmed by the direct observation of the Floquet multipliers [50], [51].

3.9. Branching technique

Once a bifurcation is localized and identified, a branching technique can be applied to transition from the main branch to the secondary one. At a bifurcation point, the uniqueness of the tangent vector $\mathbf{t}_i$, is no longer guaranteed; two distinct tangents exist, corresponding to the main and secondary branches. At this point, there exist two independent vectors $\phi = [\phi_1, \phi_2]$ solutions of $\mathbf{h_y}\phi = 0$ with $\mathbf{y} = [\mathbf{z}, \omega]$ and one left eigenvector ϕ_g to $\mathbf{h_y}$ such that $\mathbf{h_y^T}\phi_g = 0$ exists at the bifurcation. At a bifurcation point, the Jacobian matrix of the system becomes singular, resulting in a nontrivial nullspace. The first-order tangent vector $\mathbf{y_1}$, which satisfies $\mathbf{h_y y_1} = 0$, lies within this nullspace and corresponds to a direction in which the system is locally insensitive. However, this condition alone does not distinguish between the continuation of the original solution branch and the emergence of a secondary branch. Additionally, since $\mathbf{h_z}$ remains singular, it is regularized with respect to $\varphi_1 = (\nabla \otimes \mathbb{I}_n)\mathbf{z}$ such that

$$\bar{\mathbf{h}}_\mathbf{z} = \left(\mathbf{h_z} + \varphi_1\varphi_1^*\right)$$

9

To resolve this ambiguity, a second-order expansion of the solution $\mathbf{y}$ with respect to the pseudo-arclength parameter ξ is introduced:

$$\mathbf{y} = \mathbf{y_0} + \xi\mathbf{y}_1 + \xi^2\mathbf{y}_2$$
$$\mathbf{h}(\mathbf{y}) = \mathbf{h}(\mathbf{y_0}) + \xi\overline{\mathbf{h}}_\mathbf{y}\mathbf{y}_1 + \xi^2\left(\overline{\mathbf{h}}_\mathbf{y}\mathbf{y}_2 + \overline{\mathbf{h}}_{\mathbf{yy}}\mathbf{y}_1\mathbf{y}_1\right) \tag{67}$$

where $\mathbf{y}_0$ is the $(\mathbf{z}, \omega)$ at the bifurcation point, $\mathbf{y}_1$ is the first-order tangent, and $\mathbf{y}_2$ represents the curvature of the solution path. The terms of order ξ^2 are

$$\overline{\mathbf{h}}_\mathbf{y}\mathbf{y}_2 + \overline{\mathbf{h}}_{\mathbf{yy}}\mathbf{y}_1\mathbf{y}_1 = 0 \tag{68}$$

The inclusion of the second-order term is therefore essential to uniquely determine the continuation direction and ensure the trajectory departs from the original branch. Without it, the first-order information would be insufficient, as it fails to distinguish between multiple admissible paths at the bifurcation point. Equation (68) is multiplied by ϕ_g^T resulting in

$$\phi_g^T\left(\overline{\mathbf{h}}_{\mathbf{zz}}\mathbf{z_1}\mathbf{z_1} + \overline{\mathbf{h}}_{\mathbf{z}\omega}\mathbf{z_1}\omega_\mathbf{1} + \overline{\mathbf{h}}_{\omega\omega}\omega_\mathbf{1}\omega_\mathbf{1}\right) = 0 \tag{69}$$

The solution $(\mathbf{z_1}, \omega_\mathbf{1})$ is then expressed as a linear combination of two independent vectors $\phi = (\phi_1, \phi_2)$, where ϕ_1 corresponds to the null eigenvector of the Jacobian and ϕ_2 is the displacement part $\Delta\mathbf{z}$ of the tangent obtained at the previous step:

$$(\mathbf{z_1}, \omega_\mathbf{1}) = (\phi_1 + \alpha\phi_2, \alpha) \tag{70}$$

Substituting this expression into Eq. (69) yields a scalar quadratic equation in the parameter α:

$$a\alpha^2 + b\alpha + c = 0 \tag{71}$$

with

$$a = \phi_g^T\left(\left(\overline{\mathbf{h}}_\mathbf{z}\phi_2\right)_\mathbf{z}\phi_2 + 2\left(\overline{\mathbf{h}}_\mathbf{z}\phi_2\right)_\omega + \overline{\mathbf{h}}_{\omega\omega}\right)$$
$$b = \phi_g^T\left(\left(\overline{\mathbf{h}}_\mathbf{z}\phi_1\right)_\mathbf{z}\phi_2 + \left(\overline{\mathbf{h}}_\mathbf{z}\phi_1\right)_\omega\right) \tag{72}$$
$$c = \phi_g^T\left(\overline{\mathbf{h}}_\mathbf{z}\phi_1\right)_\mathbf{z}\phi_1$$

α is then simply obtained by

$$\alpha_1 = \frac{-b + \sqrt{b^2 - ac}}{a}$$
$$\alpha_2 = \frac{-b - \sqrt{b^2 - ac}}{a} \tag{73}$$

In the scenario where $c = 0$ the branch point is a pitchfork point, otherwise it is a transcritical point. Introducing α into Eq. (70) give the direction of the new tangent leading to the emerging branch.

The branching technique for the period doubling bifurcations is similar since, as stated in the previous section, the introduction of the subharmonics in the Fourier decomposition changes the nature of the bifurcation. Neimark-Sacker bifurcations are characterized by a pair of complex-conjugate Floquet exponents, λ and λ^*, for which $\Re(\lambda) = 0$ and $\frac{\partial\Re(\lambda)}{\partial\omega} \neq 0$. The eigenvector $\mathbf{v}$ associated with λ can be interpreted as the unstable mode that grows over time [52]. This allows for the construction of a predictor $\Delta\mathbf{z}$ as follows:

$$\Delta z = \begin{bmatrix} \mathbf{0} \\ -\text{sign}(\Im(\lambda))\Im(\mathbf{v}) \\ \Re(\mathbf{v}) \\ \mathbf{0} \end{bmatrix} \tag{74}$$

The additional frequency is then estimated by the imaginary part of λ.

4. Application of HBM to 433 Eros

Eros is one of the largest near-Earth objects, making it one of the most extensively studied asteroids to date. The NEAR Shoemaker probe during its mission, in 2000, provided a wealth of data on the asteroid, including detailed measurements of its topography [53] and physical characteristics [54], which have been instrumental in generating high-resolution shape models. The total mass of 433 Eros is estimated at 6.69×10^{15}kg with a bulk density, ρ, of 2.67 ± 0.03 g cm^{-3}. Its dimensions were measured as $34.4 \times 11.2 \times 11.2$ km with a volume equivalent diameter of 16.84 km and the rotation period is approximately 5.27 hours [55; 56]. When combined with the polyhedron method, these parameters allow for an accurate modeling of the gravitational environment surrounding Eros. Figure 1 displays the polyhedron model constructed from a mesh consisting of 856 vertices and 1708 faces [57].

To improve the generality and numerical conditioning of the problem, the equations of motion are adimensionalized using characteristic units of length, time, and mass. It improves numerical stability and precision by minimizing the risk of floating-point errors arising from very large or small dimensional quantities. The unit of time is chosen as the asteroid's rotation period, $t_u = 5.27 \times 3600$s, the unit length $l_u = 16.84e^3$ m and the unit mass $m_u = 6.69 \times 10^{15}$kg. It is also worth noting that the mass term cancels out due to the presence of the product $G\rho$ in equation (6).

There are four critical values of V for the particular case of 433 Eros, corresponding to the four equilibrium points. Notably, two of these points, E_1 and E_2, are saddle points, while E_3 and E_4 are center points; all are linearly unstable [58]. The positions of the equilibrium points are obtained by solving $\nabla V = 0$, their coordinates are listed in Table 1 and are displayed in Figure 4.

4.1. Impact of the number of harmonics

The Jacobi constant (Eq. (8)) is determined by the characteristics and geometry of the orbits, serving as a valuable tool for distinguishing between them. However, this conservation
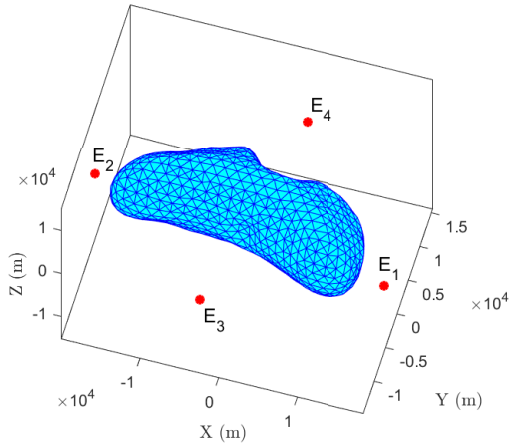
Figure 4: Position of the equilibrium points with respect to 433 Eros.

Table 1: Position of the four equilibrium points around 433 Eros.

| Equilibrium point	x (km)	y (km)	z (km)
E_1	18.444	-5.68	0.193
E_2	-19.993	-0.075	0.162
E_3	2.886	14.428	-0.015
E_4	-2.7	-13.697	-0.027

property is preserved in numerical solutions obtained through direct time integration such as Runge-Kutta schemes found in MATLAB's ode solvers. For periodic orbits computed using the HBM, small oscillations in the Jacobi constant are typically observed along the orbit. These oscillations arise due to the inherent approximation in HBM, which represents the solution as a truncated Fourier series. Specifically, the state variables (position and velocity) are approximated as sums of harmonics up to a prescribed order, N_H. Because the Jacobi constant depends nonlinearly on both position and velocity, any approximation error in these quantities translates into deviations from perfect conservation. The presence of oscillations in the Jacobi constant is therefore a direct consequence of the truncation of the harmonic expansion. The HBM solution satisfies the governing equations in an averaged sense, rather than pointwise over time. As such, the method does not enforce conservation laws exactly at each point in time, and this leads to slight periodic variations in the computed Jacobi constant. The amplitude of these oscillations decreases as the number of harmonics included in the approximation is increased. A higher number of harmonics enables the HBM to better capture the nonlinearities present in the system dynamics, leading to a more accurate reconstruction of the periodic orbit. Consequently, the approximation of the Jacobi constant improves, and the oscillations diminish in amplitude.

The global features of the periodic orbit — such as its geometry, stability type, and position in phase space — remain in good agreement with those obtained via time integration. When only a few harmonics are retained, the method primarily

captures the dominant frequency content of the orbit. For many low- to moderate-amplitude periodic orbits in the CRTBP, a large proportion of the solution energy is contained in the first few harmonics. As a result, even a low-order HBM approximation can represent the general shape and timing of the orbit reasonably well. In contrast, the Jacobi constant involves nonlinear combinations of velocity and position, which are sensitive to small inaccuracies in the higher-frequency components. Consequently, even small truncation errors in the harmonic expansion — negligible in terms of trajectory shape — can result in perceptible deviations in the computed Jacobi constant. This effect is illustrated in Figure 5 which compares the trajectories and the time evolution of the Jacobi constant obtained using 15 and 30 harmonics with a reference solution computed through time integration using MATLAB's ode113 solver.
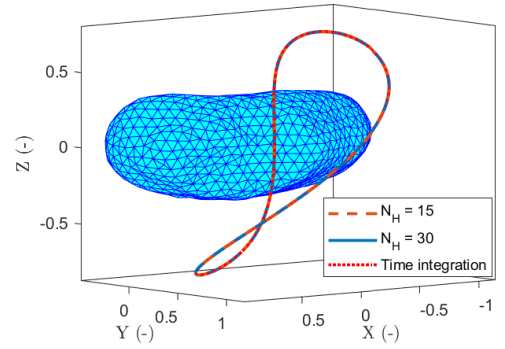
(a)
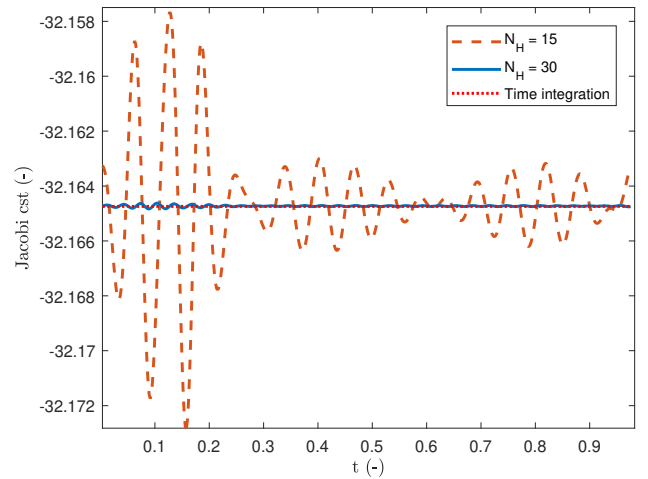
(b)

Figure 5: Comparison of 3D orbit computed with the HBM with 15 and 30 harmonics and time integrated solution with ode113 solver (a) Comparison of the evolution of the Jacobi constant computed with the HBM with 15 and 30 harmonics and time integrated solution with ode113 solver (b).

To compensate for the oscillations observed in the Jacobi constant when using the HBM, the median value of the Jacobi constant over one orbit period is used as a reference. This approach provides a robust and representative estimate of the true constant, minimizing the influence of transient numerical artifacts that can disproportionately affect the mean. The median is particularly well-suited in this context due to the symmetric nature of the oscillations around the underlying value, especially when a sufficient number of harmonics is included. This reference value enables consistent comparison with time integration results. For future results, a total of 30 harmonics were considered in the Fourier decomposition to mitigate the errors of the Jacobi constant. Furthermore, to guarantee the periodicity of the solution, the accuracy of the HBM is enforced by requiring that the residual of Eq. (23) remains below $\epsilon = 10^{-12}$.

4.2. Impact of the mesh

The HBM is compatible with asteroid models represented by meshes of various densities and shapes. However, the resolution of the mesh directly affects computational cost—denser meshes significantly increase the time required to construct families of periodic orbits. When the goal is to identify general orbit shapes rather than highly precise trajectories, reducing the number of faces in the mesh can greatly speed up the computation, albeit at the expense of accuracy. Since HBM requires an initial guess for the orbit to begin the correction process, the ability to explore a wide range of orbit types at lower computational cost is a notable advantage. To illustrate how mesh simplification affects both CPU time and solution accuracy, four different mesh resolutions are considered in this study. The original model contains 1708 faces [59], and three progressively coarser versions are generated with 1200, 298, and 30 faces, respectively (see Figure 6).
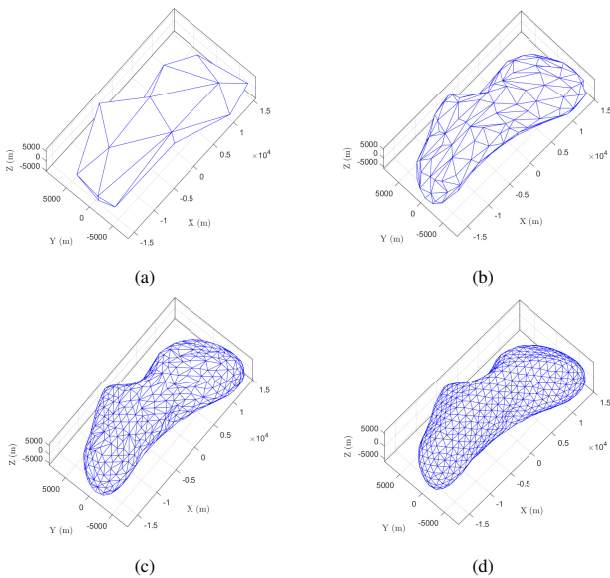
Figure 6: 3D surface mesh of asteroid 433 Eros with 17 vertices and 30 faces (a), with 151 vertices and 298 faces (b), with 602 vertices and 1200 faces (c), with 856 vertices and 1708 faces (d).

Two distinct orbits are analyzed: one primarily confined to the equatorial plane, and another exhibiting a more complex three-dimensional structure with a noticeable vertical component. The results of orbit propagation using the four mesh resolutions are compared in Figure 7. For the planar orbit, all four meshes produce converged solutions that are extremely close to one another. The solution obtained with the coarsest mesh shows a slight deviation but still captures the essential dynamics. In contrast, for the orbit with vertical motion, discrepancies become more evident in the results from the two lower-resolution meshes. Nevertheless, even these coarser meshes manage to reproduce the overall orbit shape, making them suitable for generating initial guesses that can be refined with higher-resolution models. Initial guesses are obtained either from the literature [60], or by adjusting the initial Fourier coefficients. For example, a simple circular orbit can be readily expressed in terms of Fourier coefficients, which, after a few corrective steps, provides a suitable starting point for continuation.

Computation time is largely insensitive to the orbit type but is strongly influenced by the mesh resolution. Table 2 summarizes the average time per correction step and per full iteration leading to convergence. These two metrics are reported separately, as mesh resolution also affects tasks such as stability analysis and continuation prediction, which contribute to the total iteration time. All computations were carried out using MATLAB R2020a on a Intel(R) Core(TM) i9-9900K CPU at 3.60GHz, with 32Go RAM. From Table 2, it is evident that reduced-resolution meshes significantly improve performance. The 30- and 298-face meshes yield speedups of approximately 3.84× and 2.74×, respectively, compared to the full 1708-face mesh. A smaller but still notable difference is observed between the 1200- and 1708-face meshes, with negligible differences in the resulting orbits. This demonstrates that combining HBM with mesh simplification offers an effective strategy for quickly exploring families of periodic orbits. Promising candidates identified using coarse meshes can then be used as initial conditions for higher-resolution refinement.

Table 2: Computation time per correction and iteration for the different mesh refinements.

Mesh	CPU time/correction (s)	CPU time/iteration (s)
30 Faces	≈ 1.27	≈ 3.69
298 Faces	≈ 1.72	≈ 5.17
1200 Faces	≈ 3.35	≈ 9.95
1708 Faces	≈ 4.56	≈ 14.2

4.3. Periodic orbits around 433 Eros

A wide variety of periodic orbits coexist in the vicinity of irregular celestial bodies. The Harmonic Balance Method (HBM) provides a powerful framework for identifying these solutions and constructing a comprehensive bifurcation map. Figure 8 illustrates such a map, where the Jacobi constant is plotted against the orbital period. This representation reveals the presence of all three primary bifurcation types, with
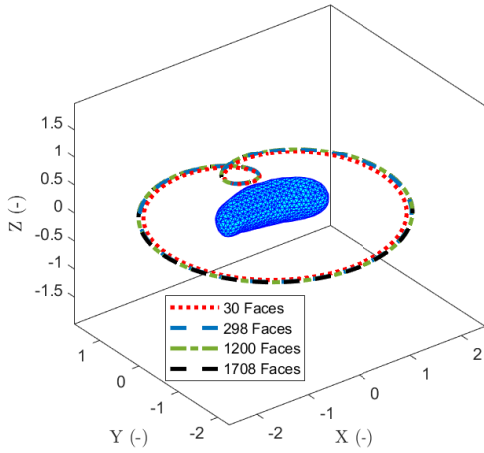
(a)
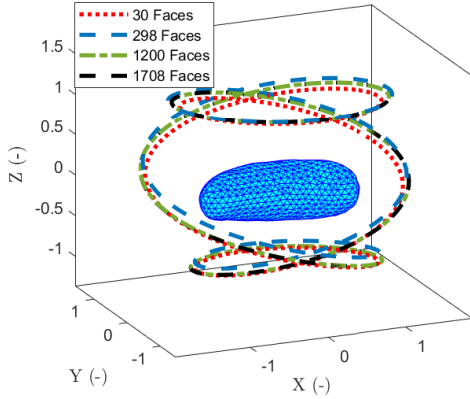
(b)

Figure 7: Comparison of planar orbit computed with the four different meshes (a). Comparison of 3D orbit computed with the four different meshes (b).

corresponding branches tracked across the diagram. Notably, while multiple period-doubling bifurcations are identified, only a single branch point is observed. The majority of periodic orbits around 433 Eros are found to be unstable. Several examples presented in this section have also been reported in prior studies using time-domain approaches [61]. Let's note that 30 harmonics were considered in order to fully capture the dynamics of the different periodic orbits.

Given the large number of periodic solutions identified through the HBM, a selection of a few of the orbits had to be made to highlight how the continuation led to dynamically rich orbits. To enhance the visualization of the connections between these branches, a deconstructed version of Figure 8 is provided in Figure 9. This schematic representation highlights the structure of the bifurcation network: dashed lines indicate branches emerging from period-doubling bifurcations, while dotted lines represent secondary branches that originate from
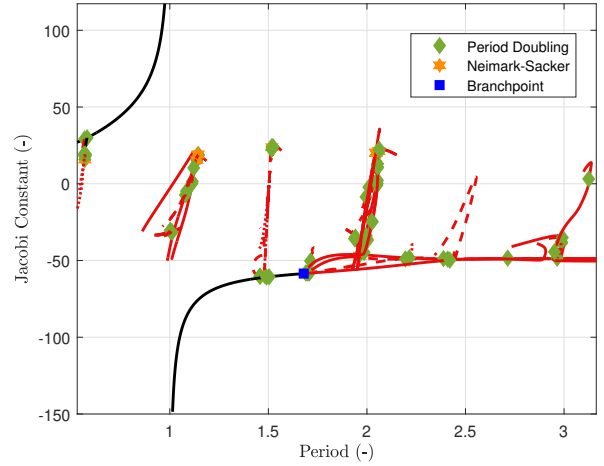
Figure 8: Continuation of stable (in black) and unstable (in red) periodic orbits around 433 Eros.

bifurcations on already period-doubled solutions. The color coding follows the convention where black lines denote stable orbits and red lines correspond to unstable ones. The symbol "//" is used to indicate gaps in the continuation between pairs of branches with nearly identical Jacobi constants and orbital periods, suggesting similar orbital geometries, either around different equilibrium points or shifted in space but not connected with bifurcations. It is worth noting that the initial conditions for branches beyond a gap are obtained by deliberately overshooting the prediction of a solution from the preceding branch. The bifurcations are denoted as period doubling (PD), Neimark–Sacker (NS), or branch point (BP).

The irregular shape of asteroid 433 Eros results in a highly non-uniform gravitational field, making the classification of well-defined orbital families challenging. In 2019, Jiang presented few families around the equilibrium points of irregular bodies [62]. The simplest class of orbits is the planar circular orbit. However, even this basic configuration exhibits two distinct variants around 433 Eros. Since the asteroid rotates counterclockwise, circular orbits may rotate either in the opposite direction (clockwise), called *retrograde*, or in the same direction (counterclockwise), called *prograde*. It is important to note that in the rotating frame fixed to Eros, both orbit families appear as prograde. The NEAR-Shoemaker probe was placed in particular on a near-circular polar orbit [63]. All subsequent three-dimensional representations of the orbits are presented in this rotating reference frame. In order to not overflow this paper with 3D representations of orbits around 433 Eros, a sample of several orbits found in the bifurcation map are presented in the annexes.
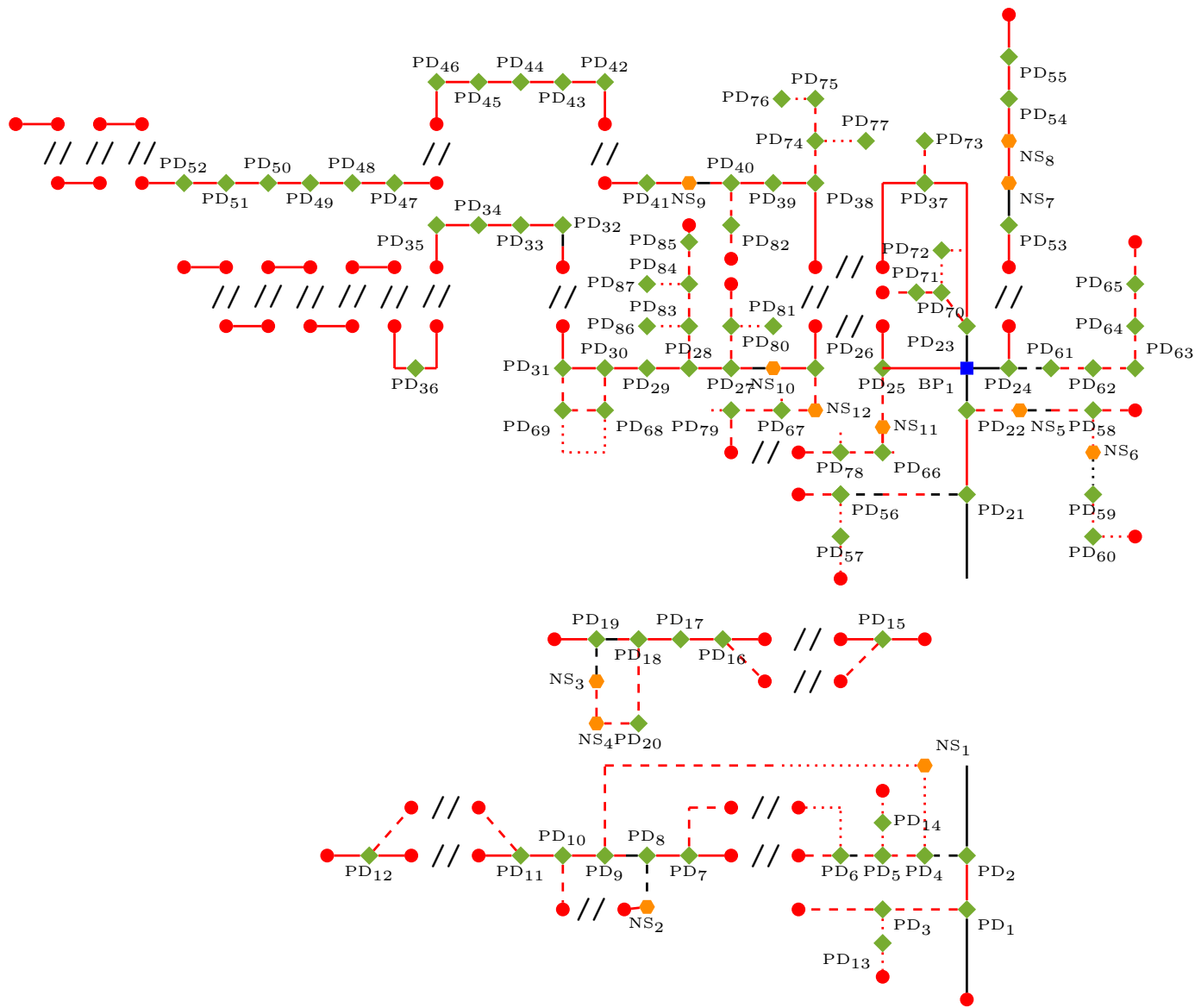
Figure 9: Schematic bifurcation map for 433 Eros.

Compared to classical time integration method, the HBM offers a powerful additional perspective for analyzing the dynamics of orbit families. In particular, it enables the study of how bifurcations influence the evolution of solutions during continuation by examining the behavior of the normalized Fourier coefficients, denoted σ_i^j:

$$\sigma_i^j = \frac{\Phi_i^j}{\sum_{i=0}^{N_H} \Phi_i^j}$$

with

$$\Phi_i^j = \sqrt{\left(s_i^{f_{xj}}\right)^2 + \left(c_i^{f_{xj}}\right)^2} \quad (j = 1, ..., n; i = 0, ..., N_H)$$

where $\Phi^j i$ represents the amplitude of the i-th harmonic in the j-th degree of freedom, and $\sigma^j i$ expresses its normalized contribution relative to the total harmonic content. The analysis focuses on a particular circular orbit family that exhibits two period-doubling bifurcations, PD_1 and PD_2, each marking a change in stability along the continuation path. The secondary branch that emerges from PD_1, which includes another bifurcation (PD_3), is also investigated, along with the new branch that arises from PD_3. These bifurcating branches are compared with the main circular family to highlight the changes in harmonic content and dynamics. Figure 10 shows the three sets of orbits in the spatial context of asteroid 433 Eros. Figure 11 presents a heat map of the normalized Fourier coefficients σ_i^j for the first 10 harmonics in the X and Y directions across the entire continuation. The positions of the period-doubling bifurcations are indicated by green lines, clearly marking where changes in harmonic structure and orbital stability occur.

(a)

(b)

(c)
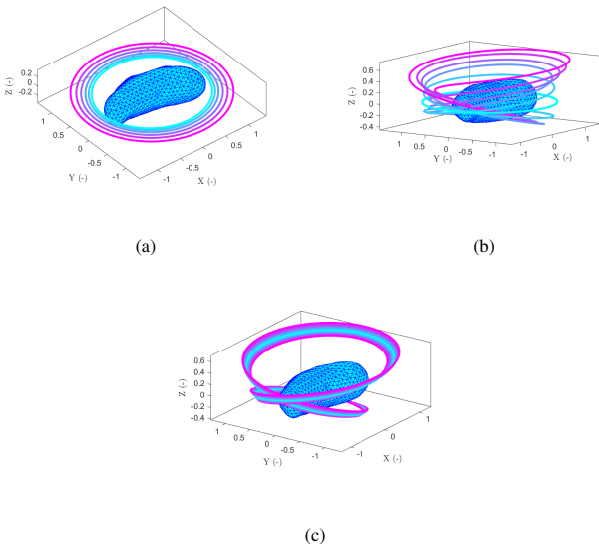
Figure 10: Quasi cicular orbits including the period doubling bifurcations PD_1 and PD_2 (a). Vertical orbits resulting from PD_1 including the period doubling bifurcation PD_3 (b). Vertical orbits resulting from PD_3 (c).

As expected, the Fourier coefficients for the circular orbit family show dominant activity in the first harmonic for both the X and Y degrees of freedom. A smaller contribution from the third harmonic in the X direction is also observed. Given that the bifurcated orbits in Figure 10(b) exhibit vertical deviations from the circular family, it is particularly relevant to examine the harmonic content in the Z direction, as shown in Figure 12. This heat map reveals a clear signature of the period-doubling bifurcation, marked by a noticeable increase in the second harmonic near the PD bifurcations. Following this bifurcation, the second harmonic becomes dominant, particularly immediately after the transition.

Concerning the orbits in Figure 10(b), the dominant harmonic is the second one, around the 60th orbit in the continuation, the third harmonic begins to show increased activity, and shortly after PD_3, the fourth harmonic becomes significant as well. Figure 13 offers a comparison of the orbits in Figure 10(b) before and after the 60th orbit. Prior to this point, the orbits primarily show increasing vertical excursion along the Z axis. Beyond the 60th orbit, however, the vertical growth is accompanied by noticeable deviations in the X and Y directions, suggesting a shift in the orbit structure.

The final family of orbits emerging after PD_3, represented in Figure 10(c), is predominantly governed by the fourth harmonic. Nonetheless, the second harmonic retains a non-negligible presence, indicating that these orbits share certain dynamical features with those just prior to the bifurcation. This evolution of the harmonic structure underscores the power of HBM in capturing subtle qualitative transitions in orbital dynamics.

5. Resonant orbits around 433 Eros

Resonances are observed in the dynamics around 433 Eros. This phenomenon is clearly visible in Figure 8, where the Jacobi constant exhibits distinct increases at integer dimensionless period values, and the associated orbital shapes tend to deviate from the equatorial plane. It is worth noting that the dashed lines—representing period doubling bifurcations—have their period halved for visualization purposes; their actual periods correspond to integer values on Figure 8. Since most of the orbits with period ratios below 3 were extensively described in the previous section, the focus here shifts to those with period ratios greater than 3. On the bifurcation map, Figure 9, these orbits correspond to a series of parallel branches, beginning with those associated with PD32 and PD42. Although the bifurcations encountered along these branches are labeled, they are not analyzed in detail, as the efficacy of the HBM in tracking bifurcations has already been demonstrated. Generally, each of these branches originates at a resonant orbit. As the period increases, the orbits tend to align with the equatorial plane. However, when the period approaches another integer value, the Jacobi constant increases and a vertical component emerges in the orbit. These vertically extended resonant orbits are the focus of this section.
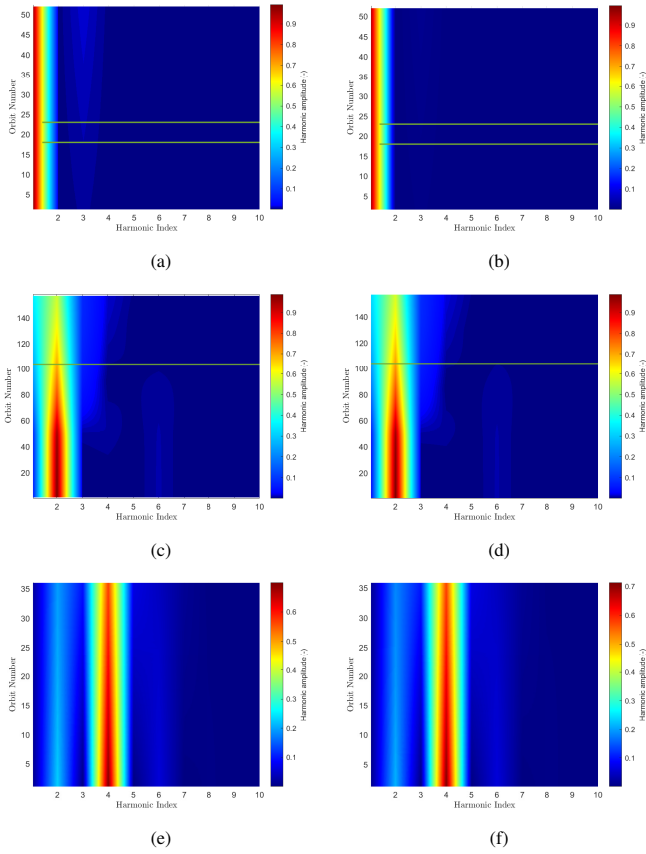
15

(a)

(b)

(c)

(d)

(e)

(f)

Figure 11: Normalized Fourier coefficients of the quasi cicular orbits including the period doubling bifurcations PD$_1$ and PD$_2$ of x (a) and y (b). Normalized Fourier coefficients of the vertical orbits resulting from PD$_1$ including the period doubling bifurcation PD$_3$ of x (c) and y (d). Normalized Fourier coefficients of the vertical orbits resulting from PD$_3$ of x (e) and y (f).
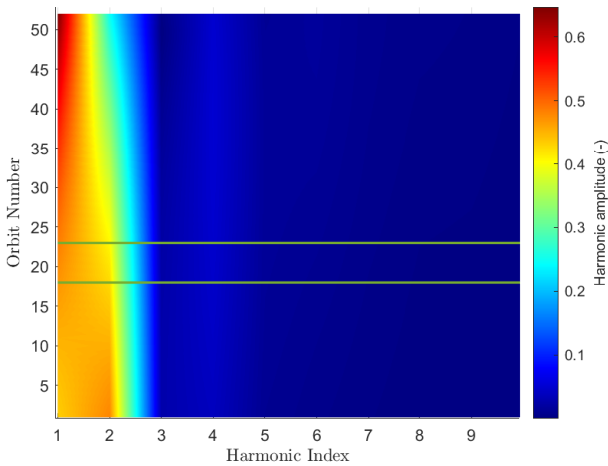

Figure 12: Normalized Fourier coefficients of the quasi cicular orbits including the period doubling bifurcations PD$_1$ and PD$_2$ of z

Figure 14 presents examples of resonant orbits corresponding to various period ratios: 1:4, 1:6, 1:8, and 1:10. In a resonance of the form n:m, the asteroid completes m rotations about its principal axis of inertia while the massless particle

(a)

(b)
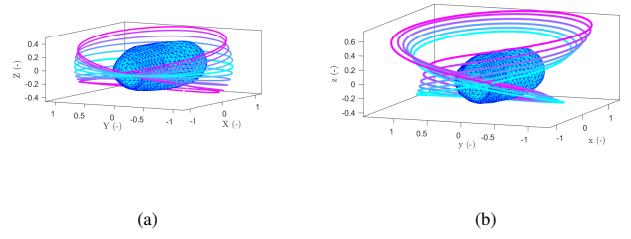
Figure 13: Decomposition of the vertical orbits resulting from PD$_1$ including the period doubling bifurcation PD$_3$. Before orbit 60 (a), after orbit 60 (b).

performs n revolutions around it. Several observations can be made about the morphology of these resonant orbits. First, they closely resemble the Heart-like family discussed earlier, with the addition of vertical loops near the equilibrium point E$_3$. Second, although the period ratios differ, the overall shape of the orbits remains qualitatively similar. The main distinction lies in the number of vertical loops: higher-period orbits tend to feature more loops, which accounts for their longer durations.
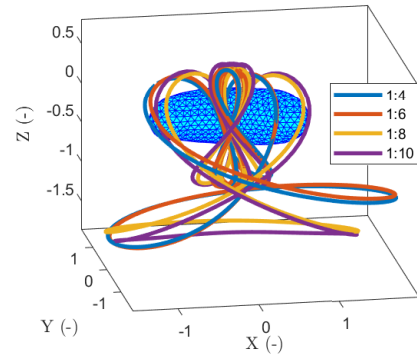
Figure 14: Example of resonant orbits around 433 Eros.

Figures 8 and 9 reveal that two consecutive resonant peaks are connected through a transition involving planar orbits. The harmonic balance method (HBM) facilitates a spectral analysis of these transitions by examining the evolution of the normalized Fourier coefficients. The transitions between the 5:1 and 6:1 resonances, as well as between the 9:1 and 10:1 resonances, are shown in Figures 15 and 17, with their corresponding spectral decompositions illustrated in Figures 16 and 18.

From these analyses, several patterns emerge. First, the transition between the 9:1 and 10:1 resonances involves a broader and more complex spectrum of harmonics than the 5:1 to 6:1 case, which reflects the increasing geometrical intricacy of higher-order resonant orbits. In both transitions, the z-

16

component of the motion exhibits a clear shift in the dominant harmonic—moving from the 5th to the 6th and from the 9th to the 10th harmonic respectively—demonstrating the spectral signature of the change in resonance. As the orbits pass through the equatorial plane during the transition, the contribution of the lower-order harmonics becomes more prominent in all three degrees of freedom, especially in the x and y directions. Additionally, the x and y components show noticeable activation of higher harmonics, particularly the 10th and 12th during the 5:1–6:1 transition and the 18th and 20th during the 9:1–10:1 transition. These contributions further emphasize the increased harmonic richness associated with more complex orbital geometries near higher-order resonances.
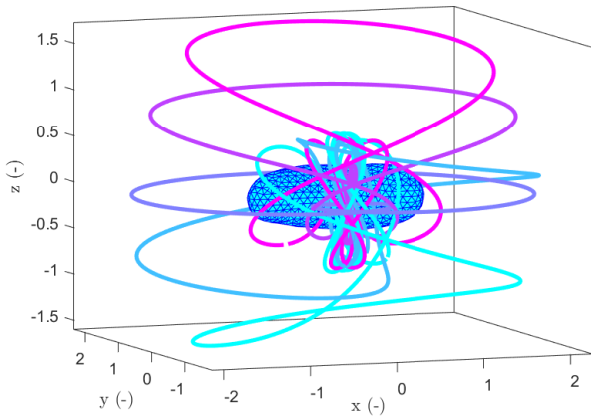
Figure 15: Transition of 5:1 resonant orbits to the 6:1 resonant orbits.

6. Quasi-periodic orbits around 433 Eros

Quasi-periodic orbits are notoriously difficult to compute using traditional numerical methods. Over long propagation times, especially for unstable solutions, numerical errors can accumulate and lead to inaccurate results. In contrast, the MHBM inherently preserves the quasi-periodic structure of the solutions, offering a robust alternative for their computation.

Identifying quasi-periodic orbits requires substantial computational effort. Although twelve distinct Neimark–Sacker bifurcations have been detected in this study, not all were pursued due to the complexity involved. Notably, to the best of our knowledge, vertical quasi-periodic orbits around 433 Eros have not yet been explored, despite this asteroid being among the most extensively studied. This work focuses on one particular Neimark–Sacker bifurcation, labeled NS_{10}, which is not a consequence of a period-doubling bifurcation. The resulting quasi-periodic orbit is shown in Figure 19.

To validate the result obtained via MHBM, the decomposed motion along the x, y, and z directions is compared to a time integration performed using MATLAB's `ode113` solver
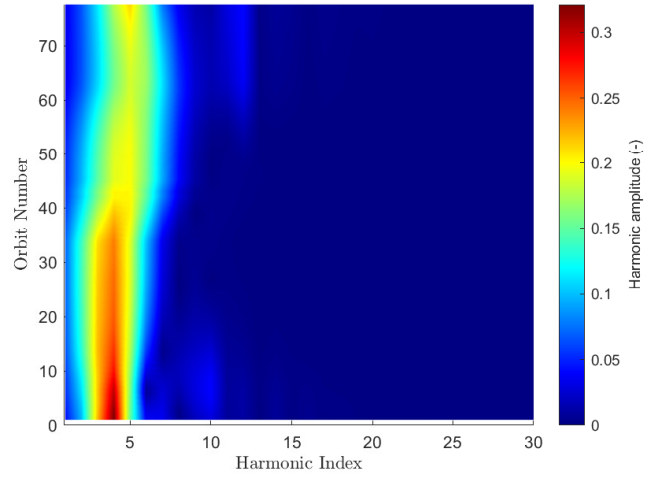
(a)
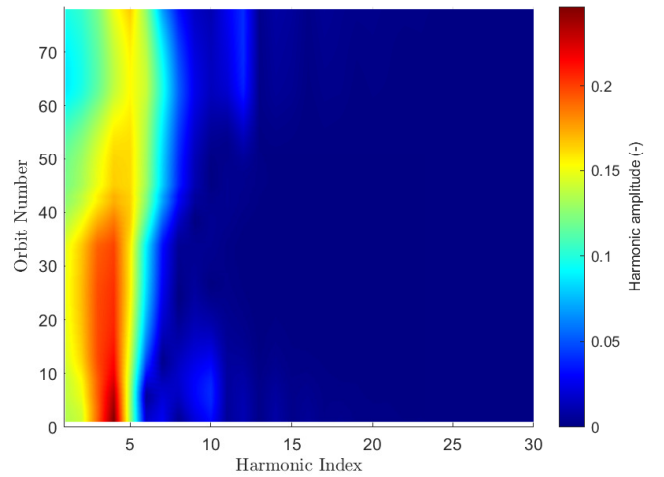
(b)
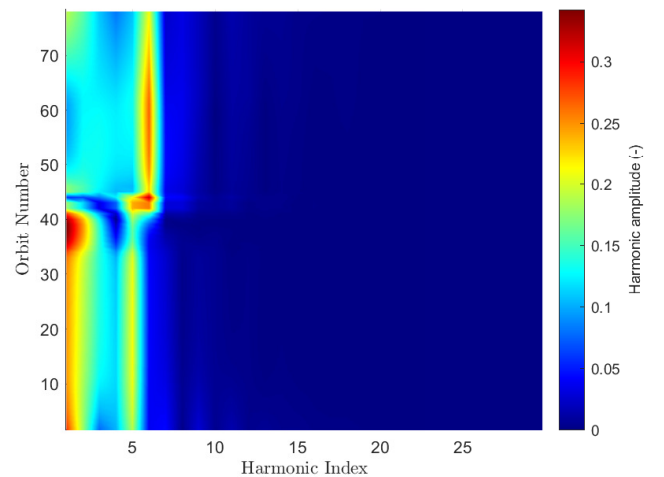
(c)

Figure 16: Normalized Fourier coefficients of the transition of the resonances 5:1 to the 6:1 of x (a), y (b) and z (c).
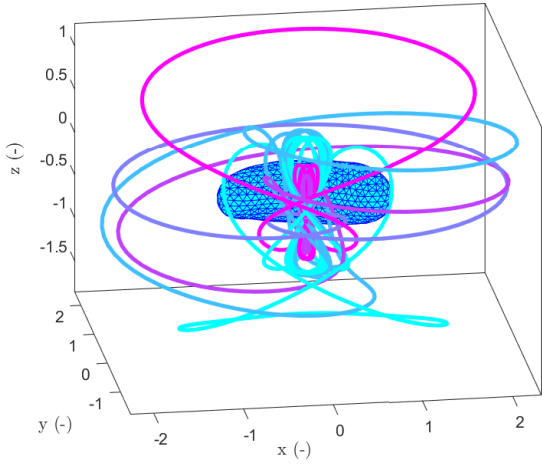
17

Figure 17: Transition of 9:1 resonant orbits to the 10:1 resonant orbits.

over one period of the second frequency, $\frac{2\pi}{\omega_2}$ (see Figure 20). The two solutions are in excellent agreement, confirming the accuracy of the MHBM. The quasi-periodic nature of the orbit is especially evident in the x and y directions. It is worth noting that this particular orbit is unstable. The solution was computed using 20 harmonics for the first frequency and 10 for the second. As previously mentioned, obtaining quasi-periodic solutions with MHBM is computationally intensive: in this case, the solution required approximately 45 minutes[1] to converge and have its stability determined.

To illustrate the sensitivity of time-domain numerical integration for quasi-periodic solutions, two different sets of initial conditions—listed in Table 3—are considered. These sets are derived from quasi-periodic orbits computed with different harmonic resolutions. The first corresponds to a solution obtained using 20 harmonics on the first frequency and 5 on the second, while the second (taken as the reference for relative error computation) results from a higher-resolution solution using 80 harmonics on the first frequency and 5 on the second.

Despite the difference in harmonic content, the solutions computed in the frequency domain using MHBM are nearly identical, as the method enforces quasi-periodicity by construction. However, when these initial conditions are propagated in time using a classical numerical integrator (Figure 21), the solution derived from the lower-harmonic approximation gradually diverges from the reference over several periods. This divergence highlights the sensitivity of traditional time-domain methods to small discrepancies in initial conditions, especially for unstable orbits. In contrast, the frequency-domain framework provided by HBM and MHBM offers a much more robust and reliable environment for studying such solutions.
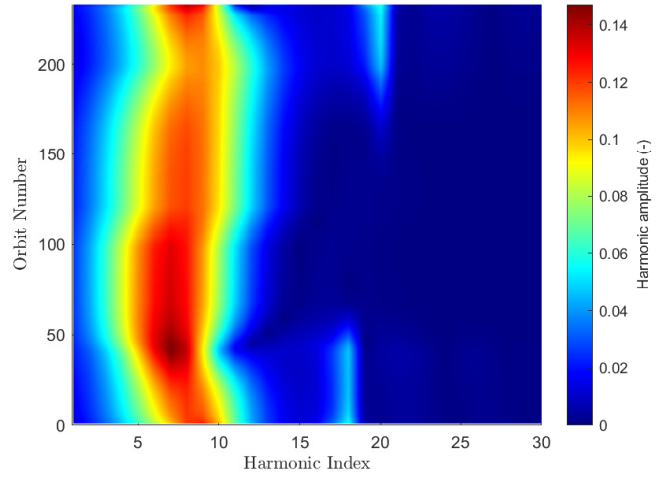
(a)
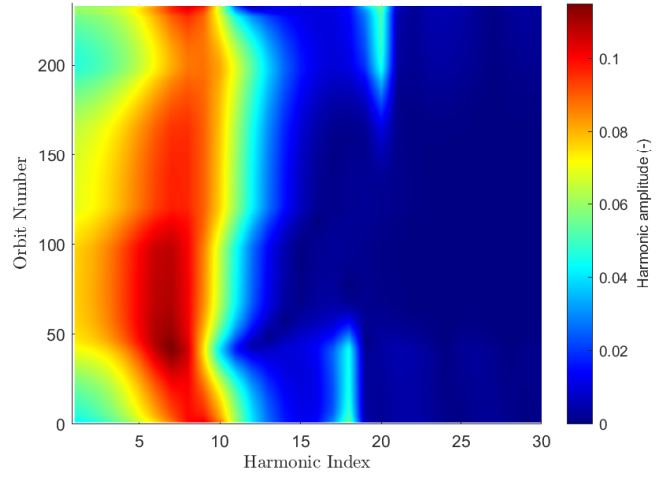
(b)
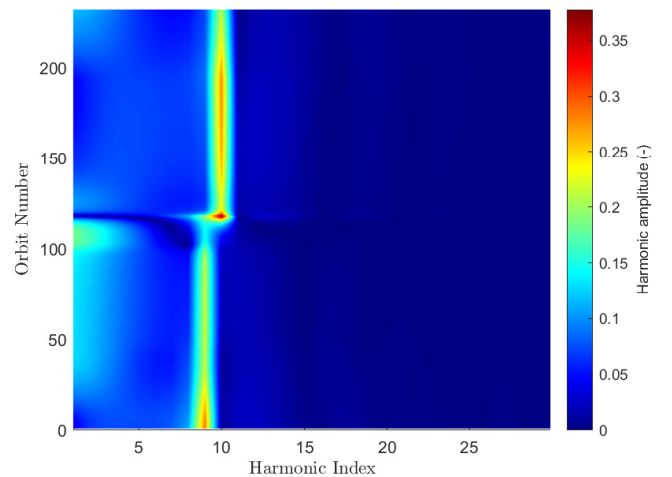
(c)

Figure 18: Normalized Fourier coefficients of the transition of the resonances 9:1 to the 10:1 of x (a), y (b) and z (c).

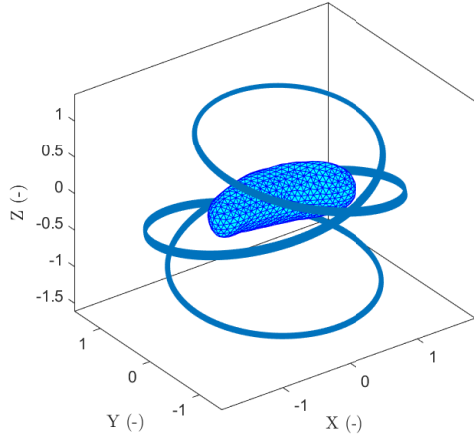[1] Intel(R) Core(TM) i9-9900K CPU at 3.60GHz, with 32GB RAM, MAT-LAB R2020a

Figure 19: Quasi-periodic orbit around 433 Eros resulting from the Neimark Sacker bifurcation NH$_{10}$.
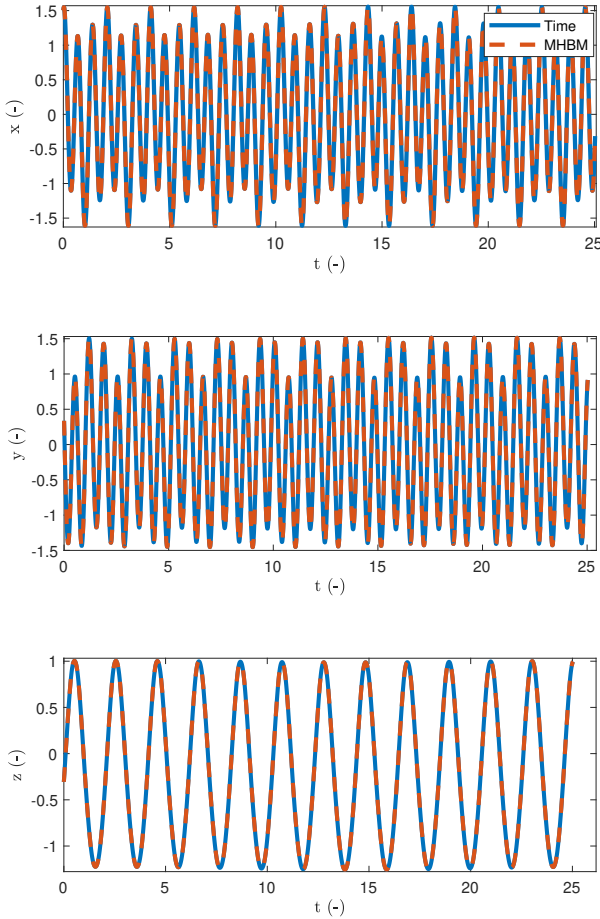

Figure 20: Comparision of the evolution of the three degrees of freedom over time computed with MHBM (NH$_1$ = 20 and NH$_2$ = 10) and time integration with `ode113` for x (a), y (b) and z (c)

Table 3: Position of the four equilibrium points around 433 Eros.

Coordinate	Initial condition 1 (-)	Initial condition 2 (-)	Relative error (%)
$\mathbf{x}_0$	1.5106	1.5073	0.2184
$\mathbf{y}_0$	0.3153	0.3361	6.1702
$\mathbf{z}_0$	-0.2842	-0.30602	7.1171
$\mathbf{v}_{x0}$	2.9441	3.1102	5.3397
$\mathbf{v}_{y0}$	-12.6162	-12.5755	0.3235
$\mathbf{v}_{z0}$	3.3842	3.3571	0.8073
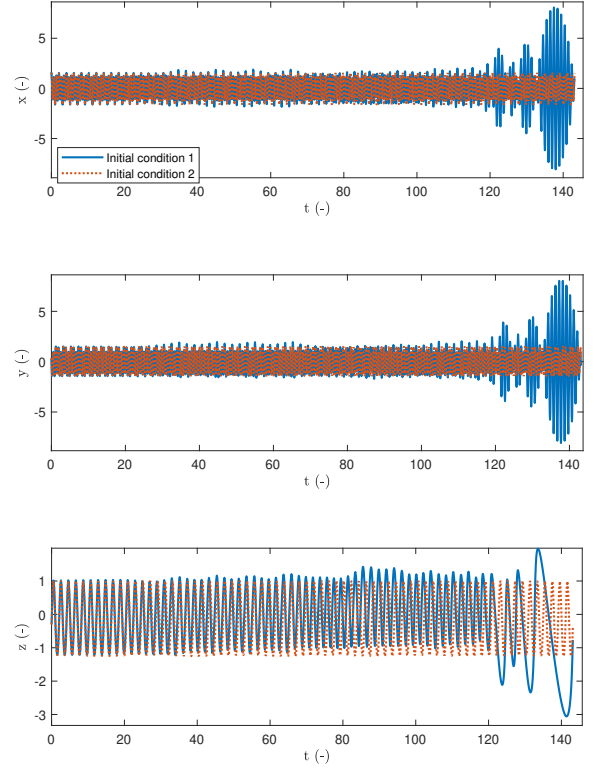
Figure 21: Comparison of the evolution of the three degrees of freedom over time for two different set of initial conditions propagated with `ode113` for x (a), y (b) and z (c)

quasi-periodic orbits around irregular bodies, using asteroid 433 Eros as a case study. Compared to conventional time-domain integration, HBM offers several key advantages: it avoids the accumulation of numerical errors, enables direct access to steady-state solutions, and provides spectral insight into orbital dynamics via the Fourier decomposition of motion. This frequency-domain approach is particularly advantageous for tracing families of periodic orbits, detecting and characterizing bifurcations, and examining transitions between resonant states.

The study also highlights the adaptability of HBM to different levels of mesh resolution, showing that reduced models can serve as efficient proxies for exploration without compromising the overall orbital geometry. Furthermore, the application of the Multi-Harmonic Balance Method (MHBM) enabled the computation of quasi-periodic orbits—an otherwise challenging task in the time domain—offering a reliable and precise

7. Summary and conclusions

This work demonstrates the capability and efficiency of the Harmonic Balance Method (HBM) in computing periodic and

alternative for analyzing complex motion in multi-frequency regimes.

Overall, HBM provides a robust and scalable framework for studying the dynamics near small celestial bodies, making it a valuable tool for mission design, stability analysis, and dynamical systems research.

References

[1] M. G. G. T. Taylor, N. Altobelli, B. Buratti, and M. Choukroun, "The rosetta mission orbiter science overview: the comet phase," *Philosophical Transactions of the Royal Society A: Mathematical, Physical and Engineering Sciences*, vol. 375, no. 2097, p. 20160262, 2017.

[2] D. Y. Oh, S. Collins, T. Drain, W. Hart, T. Imken, K. Larson, D. Marsh, D. Muthulingam, J. S. Snyder, D. Trofimov, *et al.*, "Development of the psyche mission for nasa's discovery program," 2019.

[3] H. F. Levison, C. B. Olkin, K. S. Noll, S. Marchi, J. F. Bell III, E. Bierhaus, R. Binzel, W. Bottke, D. Britt, M. Brown, M. Buie, P. Christensen, J. Emery, W. Grundy, V. E. Hamilton, C. Howett, S. Mottola, M. Pätzold, D. Reuter, J. Spencer, T. S. Statler, S. A. Stern, J. Sunshine, H. Weaver, and I. Wong, "Lucy mission to the trojan asteroids: Science goals," *The Planetary Science Journal*, vol. 2, p. 171, aug 2021.

[4] D. S. Lauretta, D. N. Dellagiustina, C. A. Bennett, D. R. Golish, K. J. Becker, S. S. Balram-Knutson, O. S. Barnouin, T. L. Becker, W. F. Bottke, W. V. Boynton, H. Campins, B. E. Clark, H. C. Connolly, C. Y. Drouet D'Aubigny, J. P. Dworkin, J. P. Emery, H. L. Enos, V. E. Hamilton, C. W. Hergenrother, E. S. Howell, M. R. M. Izawa, H. H. Kaplan, M. C. Nolan, B. Rizk, H. L. Roper, D. J. Scheeres, P. H. Smith, K. J. Walsh, C. W. V. Wolner, and Osiris-Rex Team, "The unexpected surface of asteroid (101955) Bennu," , vol. 568, pp. 55–60, Mar. 2019.

[5] Müller, T. G., Ďurech, J., Ishiguro, M., Mueller, M., Krühler, T., Yang, H., Kim, M.-J., O'Rourke, L., Usui, F., Kiss, C., Altieri, B., Carry, B., Choi, Y.-J., Delbo, M., Emery, J. P., Greiner, J., Hasegawa, S., Hora, J. L., Knust, F., Kuroda, D., Osip, D., Rau, A., Rivkin, A., Schady, P., Thomas-Osip, J., Trilling, D., Urakawa, S., Vilenius, E., Weissman, P., and Zeidler, P., "Hayabusa-2 mission target asteroid 162173 ryugu (1999 ju3): Searching for the object's spin-axis orientation," *AA*, vol. 599, p. A103, 2017.

[6] P. Michel, M. Kueppers, H. Sierks, I. Carnelli, A. F. Cheng, K. Mellab, M. Granvik, A. Kestilä, T. Kohout, K. Muinonen, *et al.*, "European component of the aida mission to a binary asteroid: Characterization and interpretation of the impact of the dart mission," *Advances in Space Research*, vol. 62, no. 8, pp. 2261–2272, 2018.

[7] P. Michel, M. Küppers, A. C. Bagatin, B. Carry, S. Charnoz, J. De Leon, A. Fitzsimmons, P. Gordo, S. F. Green, A. Hérique, *et al.*, "The esa hera mission: detailed characterization of the dart impact outcome and of the binary asteroid (65803) didymos," *The planetary science journal*, vol. 3, no. 7, p. 160, 2022.

[8] P. Geissler, J.-M. Petit, D. D. Durda, R. Greenberg, W. Bottke, M. Nolan, and J. Moore, "Erosion and ejecta reaccretion on 243 ida and its moon," *Icarus*, vol. 120, no. 1, pp. 140–157, 1996.

[9] R. Werner and D. Scheeres, "Exterior gravitation of a polyhedron derived and compared with harmonic and mascon gravitation representations of asteroid 4769 castalia," *Celestial Mechanics and Dynamical Astronomy*, vol. 65, pp. 313–344, 09 1996.

[10] T. G. G. Chanut, S. Aljbaae, and V. Carruba, "Mascon gravitation model using a shaped polyhedral source," *Monthly Notices of the Royal Astronomical Society*, vol. 450, pp. 3742–3749, 05 2015.

[11] Y. Jiang and X. Liu, "Equilibria and orbits around asteroid using the polyhedral model," *New Astronomy*, vol. 69, pp. 8–20, 2019.

[12] W. Hu, T. Fu, and C. Liu, "Revisiting the numerical evaluation and visualization of the gravity fields of asteroid 4769 castalia using polyhedron and harmonic expansions models," *Applied Sciences*, vol. 14, no. 10, 2024.

[13] A. Riaguas, A. Elipe, and M. Lara, "Periodic orbits around a massive straight segment," *Celestial Mechanics and Dynamical Astronomy*, vol. 73, no. 1-4, pp. 169–178, 1999.

[14] D. Scheeres, S. Ostro, R. Hudson, and R. Werner, "Orbits close to asteroid 4769 castalia," *Icarus*, vol. 121, no. 1, pp. 67–87, 1996.

[15] Y. Yu and H. Baoyin, "Generating families of 3d periodic orbits about asteroids," *Monthly Notices of the Royal Astronomical Society*, vol. 427, no. 1, pp. 872–881, 2012.

[16] D. Scheeres, "Orbital mechanics about small bodies," *Acta Astronautica*, vol. 72, pp. 1–14, 2012.

[17] Y. Jiang, H. Baoyin, and H. Li, "Periodic motion near the surface of asteroids," *Astrophysics and Space Science*, vol. 360, Nov. 2015.

[18] H. Shang, X. Wu, Y. Ren, and J. Shan, "An efficient algorithm for global periodic orbits generation near irregular-shaped asteroids," *Communications in Nonlinear Science and Numerical Simulation*, vol. 48, pp. 550–568, 2017.

[19] P. R. Krishna and J. G. Manathara, "Period-multiplying bifurcations in the gravitational field of asteroids," *Aerospace*, vol. 11, no. 4, p. 316, 2024.

[20] P. Llanos, J. Jordan, G. Hintz, M. Sanjurjo-Rivo, and P. Llanos de la Concha, "Trajectory analysis between quasi-periodic orbits and the lagrangian points around phobos," Aug. 2014. AIAA/AAS Astrodynamics Specialist Conference ; Conference date: 01-08-2014.

[21] H. Lei, C. Circi, E. Ortore, E. Condoleo, and B. Xu, "Quasi-frozen orbits around a slowly rotating asteroid," *Journal of Guidance, Control, and Dynamics*, vol. 42, no. 4, pp. 794–809, 2019.

[22] N. Baresi, D. J. Scheeres, and H. Schaub, "Bounded relative orbits about asteroids for formation flying and applications," *Acta Astronautica*, vol. 123, pp. 364–375, 2016.

[23] N. Baresi, Z. P. Olikara, and D. J. Scheeres, "Fully numerical methods for continuing families of quasi-periodic invariant tori in astrodynamics," *The Journal of the astronautical sciences*, vol. 65, pp. 157–182, 2018.

[24] N. Baresi and L. Dell'Elce, "Periodic and quasi-periodic orbits near close planetary moons," *Journal of Guidance, Control, and Dynamics*, vol. 46, no. 4, pp. 680–694, 2023.

[25] S. Karkar, B. Cochelin, and C. Vergez, "A comparative study of the harmonic balance method and the orthogonal collocation method on stiff nonlinear systems," *Journal of Sound and Vibration*, vol. 333, no. 12, pp. 2554–2567, 2014.

[26] Z. Yan, H. Dai, Q. Wang, and S. N. Atluri, "Harmonic balance methods: A review and recent developments," *CMES - Computer Modeling in Engineering and Sciences*, vol. 137, no. 2, pp. 1419–1459, 2023.

[27] A. Leung and Z. Guo, "Forward residue harmonic balance for autonomous and non-autonomous systems with fractional derivative damping," *Communications in Nonlinear Science and Numerical Simulation*, vol. 16, no. 4, pp. 2169–2183, 2011.

[28] C. Grenat, S. Baguet, R. Dufour, and C.-H. Lamarque, "Generalization of conservative nonlinear normal modes to the non-conservative equation of motion," in *ASME IDETC/CIE 2018 Conference, International Design Engineering Technical Conferences & Computers and Information in Engineering Conference*, pp. DETC2018–85799, 2018.

[29] G. W. Hill, "On the part of the motion of the lunar perigee which is a function of the mean motions of the sun and moon," 1886.

[30] T. Detroux, L. Renson, L. Masset, and G. Kerschen, "The harmonic balance method for bifurcation analysis of large-scale nonlinear mechanical systems," *Computer Methods in Applied Mechanics and Engineering*, vol. 296, pp. 18–38, 2015.

[31] A. Cardona, A. Lerusse, and M. Géradin, "Fast fourier nonlinear vibration analysis," *Computational Mechanics*, vol. 22, no. 2, pp. 128–142, 1998.

[32] R. Seydel, *Practical bifurcation and stability analysis*, vol. 5. Springer Science & Business Media, 2009.

[33] E. Doedel, A. Champneys, T. Fairgrieve, Y. A. Kuznetsov, B. Sandstede, and X. Wang, "Continuation and bifurcation software for ordinary differential equations," *FTP from pub/doedel/auto*, 1997.

[34] M. Peeters, R. Viguié, G. Sérandour, G. Kerschen, and J.-C. Golinval, "Nonlinear normal modes, part ii: Toward a practical computation using numerical continuation techniques," *Mechanical Systems and Signal Processing*, vol. 23, no. 1, pp. 195–216, 2009. Special Issue: Non-linear Structural Dynamics.

[35] F. Muñoz-Almaraz, E. Freire, J. Galán, E. Doedel, and A. Vanderbauwhede, "Continuation of periodic orbits in conservative and hamiltonian systems," *Physica D: Nonlinear Phenomena*, vol. 181, no. 1, pp. 1–38, 2003.

[36] G. VON GROLL and D. EWINS, "The harmonic balance method with arc-length continuation in rotor/stator contact problems," *Journal of Sound and Vibration*, vol. 241, no. 2, pp. 223–233, 2001.

[37] A. Dhooge, W. Govaerts, and Y. A. Kuznetsov, "Matcont: A matlab pack-

age for numerical bifurcation analysis of odes," *ACM Trans. Math. Softw.*, vol. 29, p. 141–164, June 2003.

[38] L. Chua and A. Ushida, "Algorithms for computing almost periodic steady-state response of nonlinear systems to multiple input frequencies," *IEEE Transactions on circuits and systems*, vol. 28, no. 10, pp. 953–971, 1981.

[39] Y.-B. Kim and S. Noah, "Quasi-periodic response and stability analysis for a non-linear jeffcott rotor," *Journal of Sound and Vibration*, vol. 190, no. 2, pp. 239–253, 1996.

[40] L. Guillot, P. Vigué, C. Vergez, and B. Cochelin, "Continuation of quasi-periodic solutions with two-frequency harmonic balance method," *Journal of Sound and Vibration*, vol. 394, pp. 434–450, 2017.

[41] Q. Wang, Z. Yan, and H. Dai, "An efficient multiple harmonic balance method for computing quasi-periodic responses of nonlinear systems," *Journal of Sound and Vibration*, vol. 554, p. 117700, 2023.

[42] H. Liao, Q. Zhao, and D. Fang, "The continuation and stability analysis methods for quasi-periodic solutions of nonlinear systems," *Nonlinear Dynamics*, vol. 100, pp. 1469–1496, 2020.

[43] F. Schilder, W. Vogt, S. Schreiber, and H. Osinga, "Fourier methods for quasi-periodic oscillations," *International Journal for Numerical Methods in Engineering*, vol. 67(5), pp. 629 – 671, July 2006. Publisher: John Wiley Sons Ltd.

[44] A. Lazarus, "A harmonic-based method for computing the stability of periodic solutions of dynamical systems," *Comptes Rendus Mecanique - C R MEC*, vol. 338, pp. 510–517, 09 2010.

[45] G. Moore, "Floquet theory as a computational tool," *SIAM Journal on Numerical Analysis*, vol. 42, no. 6, pp. 2522–2568, 2005.

[46] B. Meini, "A "shift-and-deflate" technique for quadratic matrix polynomials," *Linear Algebra and its Applications*, vol. 438, p. 1946–1961, 02 2013.

[47] Y. A. Kuznetsov, I. A. Kuznetsov, and Y. Kuznetsov, *Elements of applied bifurcation theory*, vol. 112. Springer, 1998.

[48] W. Govaerts, Y. Kuznetsov, V. De Witte, A. Dhooge, H. Meijer, W. Mestrom, A. Riet, and B. Sautois, "MATCONT and CL MATCONT: Continuation toolboxes in MATLAB," technical report, Gent University and Utrecht University, 2011.

[49] R. Alcorta, S. Baguet, B. Prabel, P. Piteau, and G. Jacquet-Richardet, "Period doubling bifurcation analysis and isolated sub-harmonic resonances in an oscillator with asymmetric clearances," *Nonlinear Dynamics*, vol. 98, 12 2019.

[50] L. Xie, S. Baguet, B. Prabel, and R. Dufour, "Bifurcation tracking by Harmonic Balance Method for performance tuning of nonlinear dynamical systems," *Mechanical Systems and Signal Processing*, vol. 88, pp. 445–461, May 2017.

[51] G. Hurel, S. Baguet, and C.-H. Lamarque, "Neimark sacker bifurcations and non-linear energy exchange in chains of non-linear oscillators," *International Journal of Non-Linear Mechanics*, vol. 144, p. 104057, 2022.

[52] B. Zhou, F. Thouverez, and D. Lenoir, "A variable-coefficient harmonic balance method for the prediction of quasi-periodic response in nonlinear systems," *Mechanical Systems and Signal Processing*, vol. 64-65, pp. 233–244, 2015.

[53] P. Thomas, J. Joseph, B. Carcich, J. Veverka, B. Clark, J. Bell, A. Byrd, R. Chomko, M. Robinson, S. Murchie, L. Prockter, A. Cheng, N. Izenberg, M. Malin, C. Chapman, L. McFadden, R. Kirk, M. Gaffey, and P. Lucey, "Eros: Shape, topography, and slope processes," *Icarus*, vol. 155, no. 1, pp. 18–37, 2002.

[54] J. Miller, A. Konopliv, P. Antreasian, J. Bordi, S. Chesley, C. Helfrich, W. Owen, T. Wang, B. Williams, D. Yeomans, and D. Scheeres, "Determination of shape, gravity, and rotational state of asteroid 433 eros," *Icarus*, vol. 155, no. 1, pp. 3–17, 2002.

[55] T. Chanut, O. Winter, and M. Tsuchida, "3d stability orbits close to 433 eros using an effective polyhedral model method," *Monthly Notices of the Royal Astronomical Society*, vol. 438, pp. 56–, 02 2014.

[56] Jet Propulsion Laboratory, "Jpl small-body database browser." https://ssd.jpl.nasa.gov/tools/sbdb$_{l}ookup.html/?_{s}str$ = 2000433, 2025.

[57] M. Thompson, "Raugh, a., near collected target models v1.0, near-a-5-collected-models-v1.0, nasa planetary data system, 2002.," 2022. https://pds.nasa.gov/ds-view/pds/viewDataset.jsp?dsid=NEAR-A-5-COLLECTED-MODELS-V1.0.

[58] D. Scheeres, "Dynamics about uniformly rotating triaxial ellipsoids: Applications to asteroids," *Icarus*, vol. 110, no. 2, pp. 225–238, 1994.

[59] N. J. P. Laboratory, "Three-body periodic orbits," 2024. https://ssd.jpl.nasa.gov/tools/periodic$_{o}rbits.html/intro[Accessed$: (11/12/2024)].

[60] H. Kang, Y. Jiang, and H. Li, "Pseudo bifurcation and variety of periodic ratio for periodic orbit families close to asteroid (22) kalliope," *Planetary and Space Science*, vol. 158, pp. 69–86, 2018.

[61] Y. Ni, Y. Jiang, and H. Baoyin, "Multiple bifurcations in the periodic orbit around eros," *Astrophysics and Space Science*, vol. 361, Apr. 2016.

[62] Y. Jiang and H. Baoyin, "Periodic orbits related to the equilibrium points in the potential of irregular-shaped minor celestial bodies," *Results in Physics*, vol. 12, pp. 368–374, 2019.

[63] D. Yeomans, P. Antreasian, J.-P. Barriot, S. Chesley, D. Dunham, R. Farquhar, J. Giorgini, C. Helfrich, A. Konopliv, J. McAdams, J. Miller, W. Owen, D. Scheeres, P. Thomas, J. Veverka, and B. Williams, "Radio science results during the near-shoemaker spacecraft rendezvous with eros," *Science (New York, N.Y.)*, vol. 289, pp. 2085–8, 10 2000.
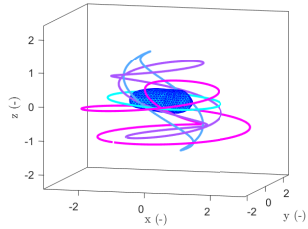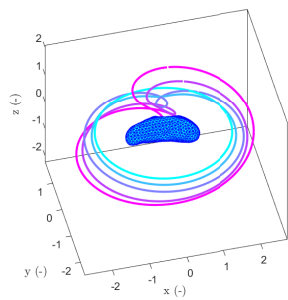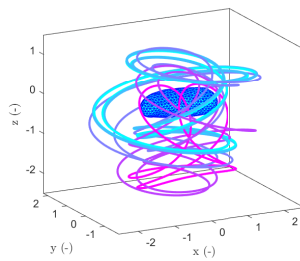
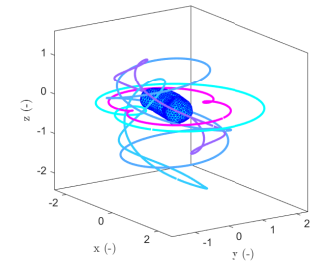(a) Family around BP$_1$.
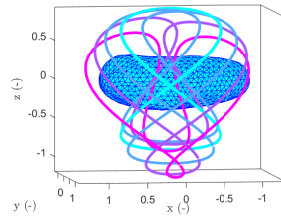
(b) Family around PD$_{10}$.
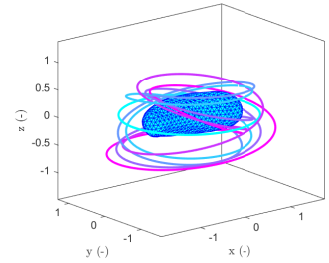
(c) Family around PD$_2$.

(d) Family around PD$_{24}$.

(e) Family around PD$_{36}$.

(f) Family around PD$_{41}$.
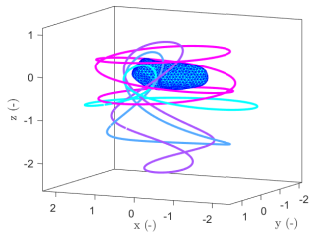
(g) Family around PD$_{54}$.
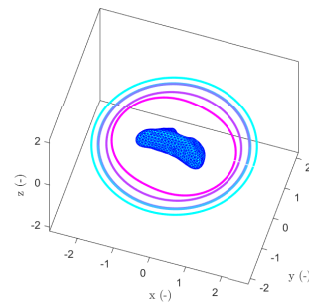
(h) Family around PD$_{36}$.
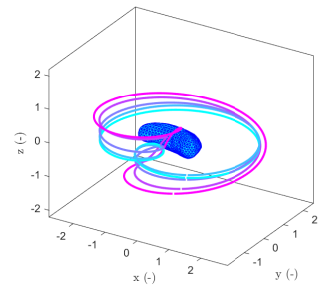
(i) Family around PD$_{26}$.
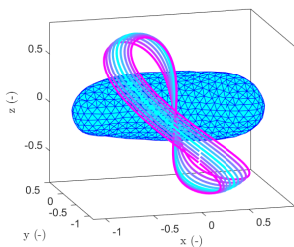
(j) Family around PD$_{15}$.
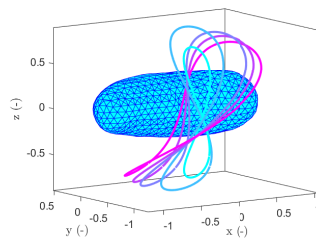
(k) Family around PD$_{16}$.
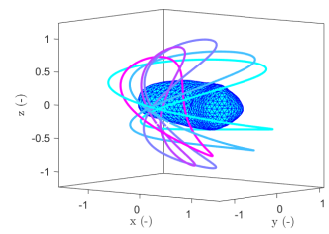
(l) Family around PD$_{19}$.

Samples of periodic orbits around 433 Eros